Monthly Notices of the ROYAL ASTRONOMICAL SOCIETY

MNRAS **506,** 1480–1497 (2021)
Advance Access publication 2021 June 24

https://doi.org/10.1093/mnras/stab1786

Jeans modelling of axisymmetric galaxies with multiple stellar populations

Caterina Caravita,[1,2★] Luca Ciotti[1] and Silvia Pellegrini[1,2]

[1]*Department of Physics and Astronomy, University of Bologna, via P. Gobetti 93/2, I-40129 Bologna, Italy*
[2]*INAF-OAS of Bologna, via P. Gobetti 93/3, I-40129 Bologna, Italy*

Accepted 2021 June 18. Received 2021 June 3; in original form 2021 February 17

ABSTRACT

We present the theoretical framework to efficiently solve the Jeans equations for multicomponent axisymmetric stellar systems, focusing on the scaling of all quantities entering them. The models may include an arbitrary number of stellar distributions, a dark matter halo, and a central supermassive black hole; each stellar distribution is implicitly described by a two- or three-integral distribution function, and the stellar components can have different structural (density profile, flattening, mass, scale length), dynamical (rotation, velocity dispersion anisotropy), and population (age, metallicity, initial mass function, mass-to-light ratio) properties. In order to determine the ordered rotational velocity and the azimuthal velocity dispersion fields of each component, we introduce a decomposition that can be used when the commonly adopted Satoh decomposition cannot be applied. The scheme developed is particularly suitable for a numerical implementation; we describe its realization within our code JASMINE2, optimized to maximally exploit the scalings allowed by the Poisson and the Jeans equations, also in the post-processing procedures. As applications, we illustrate the building of three multicomponent galaxy models with two distinct stellar populations, a central black hole, and a dark matter halo; we also study the solution of the Jeans equations for an exponential thick disc, and for its multicomponent representation as the superposition of three Miyamoto–Nagai discs. A useful general formula for the numerical evaluation of the gravitational potential of factorized thick discs is finally given.

Key words: methods: analytical – methods: numerical – galaxies: kinematics and dynamics – galaxies: structure.

1 INTRODUCTION

Axisymmetric galaxy models often represent an acceptable description of real galaxies, beyond the zeroth-order approximation of spherical symmetry. Analytical models of one and multicomponent axisymmetric galaxies are available (e.g. see Binney & Tremaine 2008, hereafter BT08, and references therein; see also Ciotti et al. 2021, hereafter CMPZ21), but these models, while important to highlight fundamental properties of the dynamics of axisymmetric systems, and to guide the construction of realistic galaxy models to be carried out numerically, suffer from the restrictions imposed by the request of analytical tractability. From this point of view, analytical and numerical modelling should be seen as complementary approaches, each of them with their own merits and limitations.

On the numerical side, the most common models are based on the solution of the Jeans equations (e.g. BT08; Ciotti 2021). This approach allows to model axisymmetric stellar systems, in the simplest assumption of a two-integral phase-space distribution function (DF; e.g. Posacki, Pellegrini & Ciotti 2013), or a three-integral DF (e.g. Cappellari 2008), starting from the assignment of the density components. As well known, the proper description of a stellar system should start from the assignment of the phase-space DF of each separate mass component, and the solution of the associated Poisson equation (BT08; Bertin 2014; Ciotti 2021); however, in several applications, the Jeans approach is highly preferred, for its direct control on the density distributions (even if it leaves open fundamental issues such as the phase-space consistency).

In this paper, we present a procedure especially designed to build (and project) multicomponent systems. For an arbitrary number of mass components, we start with maximally exploiting the scalings allowed by the Poisson and the Jeans equations, and then we show how to combine the solutions for all components to obtain a particular multicomponent model. When implemented numerically, this scheme allows for a fast and flexible building of realistic models. To provide an example, we describe how the various steps of the procedure were inserted in our code JASMINE (*Jeans AxiSymmetric Models of galaxies IN Equilibrium*; Posacki et al. 2013) for the axisymmetric modelling of galaxies based on the Jeans equations; the resulting much extended code version was named JASMINE2. This new code allows for the choice, in input, of different stellar components and dark matter (DM) components (from a continuously updated library), and a central black hole (BH). It computes numerically the gravitational potential of each density component by using the well-known formula based on complete elliptic integrals of the first kind. This numerical method is highly accurate, but it easily becomes quite time expensive, depending on the grid resolution and on the number of density components; if one wants to explore the parameter space (that can be very large, especially for multicomponent models), the possibility of a scheme to allow for a full scaling of the Poisson and the Jeans equations is crucial. The building of a model is then organized in two distinct parts: in the first one, whose numerical realization we call *Potential and Jeans Solver*, one computes the potential and then solves the

★ E-mail: caterina.caravita2@unibo.it

Jeans equations for each scaled stellar density component; this produces a set of solutions that represents a 'progenitor' of a family of models. In the second part, that in our numerical realization is seen as a *post-processing* (PP) phase, the mass and luminosity weights are assigned, and the kinematical decompositions imposed; with these, the scaled solutions of the progenitor are finally combined, and the resulting kinematical fields projected.

This procedure allows to drastically reduce the computational time needed for the construction of a multicomponent model: with a single run of the Potential and Jeans Solver, one can build a *family* of galaxy models, all characterized by the same set of scaled density components; each specific model in the family is defined by choosing suitable weights and kinematical decompositions in PP. In this way, the exploration of the parameter space is extremely fast and complete. Summarizing, each stellar density component in a multicomponent model is characterized by different structural (density profile, flattening, total mass, scale length), dynamical (rotational support, velocity dispersion anisotropy), and stellar population (age, metallicity, initial mass function, mass-to-light ratio) properties. The addition of a central BH and a DM halo is immediate.

The paper is organized as follows. Section 2 presents the analytical framework of the procedure, together with a new velocity decomposition for the azimuthal velocity field, to be used when the commonly adopted Satoh (1980) k-decomposition cannot be applied (a not uncommon case in multicomponent systems). In Section 3, we detail how the scaling is carried out. In Section 4, some illustrative galaxy models are built, and a few tests are mentioned; we also present an application to the case of the exponential disc and its decomposition as sum of Miyamoto–Nagai discs. In Section 5, the main conclusions are summarized. Finally, Appendices A and B contain some relevant analytical details.

2 MULTICOMPONENT GALAXY MODELS

In this section, we introduce the general notation used, and we illustrate the main theoretical foundations on which our modelling procedure is based; in particular, we focus on the multicomponent Jeans equations, on a generalization of the Satoh k-decomposition for azimuthal motions, and on the projections on the plane of the sky. In the following Section 3, we will describe the scaling procedure, and in particular how the scaled solutions of the Jeans equations are obtained (with the Potential and Jeans Solver), and then combined by adopting suitable weights (in the PP phase).

2.1 Structure of the galaxy models

We adopt cylindrical coordinates (R, φ, z), with the symmetry axis of the models aligned with the z-axis. In full generality, we consider models composed of N different stellar density distributions $\rho_{*i}(R, z)$, of total mass M_{*i}, so that the total stellar density ρ_* and the total stellar mass M_* of the system are given respectively by

$$\rho_*(R, z) = \sum_i \rho_{*i}, \quad M_* = \sum_i M_{*i}, \quad i = 1, \ldots, N. \tag{1}$$

From now on, sums over i indicate sums over the N stellar components. We assume that each ρ_{*i} is made of a simple stellar population (see e.g. Renzini & Buzzoni 1986; Maraston 2005), i.e. by stars of the same age, chemical composition, initial mass function, and in particular the same mass-to-light ratio Υ_{*i}. Therefore, the total stellar distribution ρ_* can be considered a composite stellar population; the luminosity density and the total luminosity of each stellar component can be written respectively as

$$\nu_{*i}(R, z) = \frac{\rho_{*i}}{\Upsilon_{*i}}, \quad L_i = \frac{M_{*i}}{\Upsilon_{*i}}, \tag{2}$$

so that

$$\nu_*(R, z) = \sum_i \nu_{*i}, \quad L = \sum_i L_i. \tag{3}$$

The local and average stellar mass-to-light ratios of the galaxy are given by

$$\Upsilon_*(R, z) \equiv \frac{\rho_*}{\nu_*} = \frac{\sum_i \rho_{*i}}{\sum_i \rho_{*i}/\Upsilon_{*i}}, \quad \langle \Upsilon_* \rangle \equiv \frac{M_*}{L} = \frac{\sum_i M_{*i}}{\sum_i M_{*i}/\Upsilon_{*i}}, \tag{4}$$

where it is apparent how in general the local stellar mass-to-light ratio in a multicomponent model depends on position.

From equation (1) the gravitational potential associated with the total stellar density is

$$\phi_*(R, z) = \sum_i \phi_{*i}, \tag{5}$$

where $\phi_{*i}(R, z)$ is the potential originated by the density component ρ_{*i}. The presence of a central BH, of mass $M_{\rm BH}$, produces the potential

$$\phi_{\rm BH}(r) = -\frac{GM_{\rm BH}}{r}, \quad r = \sqrt{R^2 + z^2}, \tag{6}$$

and an axisymmetric DM halo, of density $\rho_{\rm h}(R, z)$ and total mass $M_{\rm h}$ (when finite), produces the potential $\phi_{\rm h}(R, z)$. Therefore, in general, the total gravitational potential of the model is

$$\Phi(R, z) = \phi_* + \phi_{\rm h} + \phi_{\rm BH} = \sum_j \phi_j, \quad j = 1, \ldots, N + 2. \tag{7}$$

From now on, sums over j indicate sums over *all* the $N + 2$ galaxy components, i.e. the N stellar components, the central BH, and the DM halo. In principle, also the DM distribution can be made of different components, with a trivial generalization of the current discussion, that is not necessary for the goal of this paper. Our scheme fully exploits the linearity of the Jeans equations with respect to the stellar density (Section 2.2) and to the gravitational potential (Section 3).

2.2 The Jeans equations

The procedure, in its basic version, assumes that each stellar component is implicitly described by a two-integral phase-space DF $f_i(E, J_z)$ (in general different for each component), where E and J_z are respectively the energy and the axial component of the angular momentum of each star (per unit mass) in the *total* potential Φ. Therefore, the DF of the total stellar distribution is the two-integral function

$$f = \sum_i f_i. \tag{8}$$

As usual, we indicate with $(\mathrm{v}_R, \mathrm{v}_\varphi, \mathrm{v}_z)$ the velocity components in the phase space, and with a bar over a quantity the operation of average over the velocity space. By construction, for each stellar component $\overline{\mathrm{v}_R}_i = \overline{\mathrm{v}_z}_i = 0$, the only non-zero ordered velocity can occur in the azimuthal direction $\upsilon_{\varphi i} \equiv \overline{\mathrm{v}_\varphi}_i$, and finally for the velocity dispersion tensor $\sigma_{Ri} = \sigma_{zi} \equiv \sigma_i$. Of course, from equation (8) similar relations hold for the kinematical fields of the total ρ_*.

The Jeans equations for each stellar component are obtained as velocity averages of the collisionless Boltzmann Equation over the

corresponding f_i (e.g. BT08), so that

$$\begin{cases} \dfrac{\partial \rho_{*i}\sigma_i^2}{\partial z} = -\rho_{*i}\dfrac{\partial \Phi}{\partial z}, \\ \dfrac{\partial \rho_{*i}\sigma_i^2}{\partial R} = \rho_{*i}\dfrac{\Delta_i}{R} - \rho_{*i}\dfrac{\partial \Phi}{\partial R}, \end{cases} \tag{9}$$

where Φ is the total potential in equation (7), and

$$\Delta_i \equiv \overline{\mathrm{v}_{\varphi i}^2} - \sigma_i^2, \quad \sigma_{\varphi i}^2 = \overline{\mathrm{v}_{\varphi i}^2} - \upsilon_{\varphi i}^2 = \Delta_i + \sigma_i^2 - \upsilon_{\varphi i}^2; \tag{10}$$

therefore, in the isotropic case, $\Delta_i = \upsilon_{\varphi i}^2$. Imposing the natural boundary condition $\rho_{*i}\sigma_i^2 \to 0$ for $z \to \infty$, the solution of equations (9) is

$$\rho_{*i}\sigma_i^2 = \int_z^\infty \rho_{*i}\frac{\partial \Phi}{\partial z'}\,\mathrm{d}z', \quad \rho_{*i}\Delta_i = R\left(\frac{\partial \rho_{*i}\sigma_i^2}{\partial R} + \rho_{*i}\frac{\partial \Phi}{\partial R}\right). \tag{11}$$

We notice that Δ_i can be also recast as a commutator-like integral (e.g. see equation 35 in CMPZ21), with some advantage for analytical and numerical investigations; however, we found by several numerical tests that Δ_i can also be accurately computed by (centred) numerical differentiation as in equation (11), and so in our code JASMINE2 we maintained this more direct way of evaluation.

A central point of the procedure is the sum rule in the phase space imposed by the identity (8). In fact, with equation (8), we are assuming that the N stellar components ρ_{*i} are physically distinct, each of them described by its own f_i, and so necessarily the N pairs of equations (9) are the moment equations of each f_i in the total potential Φ. As usual, if $F(\boldsymbol{x}, \boldsymbol{v})$ is a generic dynamical property defined over the phase space, then

$$\overline{F}_i = \frac{\int F f_i\,\mathrm{d}^3\mathrm{v}}{\rho_{*i}}, \quad \overline{F} = \frac{\sum_i \rho_{*i}\overline{F}_i}{\rho_*}, \quad \overline{F}_{\mathscr{L}} = \frac{\sum_i \nu_{*i}\overline{F}_i}{\nu_*}, \tag{12}$$

where the properties $\overline{F}$ and $\overline{F}_{\mathscr{L}}$ of the galaxy can be interpreted as the *mass-weighted* and the *luminosity-weighted* averages of the $\overline{F}_i$, respectively. Notice that we are not reconstructing here the phase-space DFs of the models; we just determine the general rules of combination of the velocity moments in multicomponent systems. The previous considerations show how to combine the solution for the single ρ_{*i} to obtain the dynamical fields associated with the total ρ_*. Clearly, the Jeans equations for ρ_* in equation (1) are obtained as the sum of equations (9) over the N components, and their solution can be written as

$$\begin{cases} \sigma^2 = \dfrac{\sum_i \rho_{*i}\sigma_i^2}{\rho_*}, \quad \Delta = \dfrac{\sum_i \rho_{*i}\Delta_i}{\rho_*}, \\ \overline{\mathrm{v}_\varphi^2} = \dfrac{\sum_i \rho_{*i}\overline{\mathrm{v}_{\varphi i}^2}}{\rho_*}, \quad \upsilon_\varphi = \dfrac{\sum_i \rho_{*i}\upsilon_{\varphi i}}{\rho_*}, \end{cases} \tag{13}$$

where the previous identities are of straightforward proof from equations (12) and (10). Note that σ_φ^2 is *not* given by the simple sum of the $\sigma_{\varphi i}^2$ of the single components, as σ^2 in equation (13) above, because from equations (13) and (10) one has

$$\sigma_\varphi^2 = \overline{\mathrm{v}_\varphi^2} - \upsilon_\varphi^2 = \Delta + \sigma^2 - \upsilon_\varphi^2 = \frac{\sum_i \rho_{*i}(\sigma_{\varphi i}^2 + \upsilon_{\varphi i}^2)}{\rho_*} - \upsilon_\varphi^2. \tag{14}$$

Similarly, from equation (12), we derive all the corresponding luminosity-weighted quantities; we do not give here their expressions, since they are just obtained by using as weights the luminosity densities ν_{*i} of the components instead of the mass densities ρ_{*i}, in equations (13) and (14).

Finally, the rotation curve in the equatorial plane is given in terms of the circular velocity $\upsilon_{\mathrm{c}j}$ of each mass component as

$$\upsilon_\mathrm{c}^2 = \sum_j \upsilon_{\mathrm{c}j}^2. \tag{15}$$

2.3 Azimuthal velocity decomposition

As well known, equations (9) are degenerate in the azimuthal direction, i.e. they only provide $\overline{\mathrm{v}_{\varphi i}^2} = \sigma_{\varphi i}^2 + \upsilon_{\varphi i}^2$. The most common phenomenological approach to break this degeneracy is the Satoh (1980) k-decomposition. If $\Delta_i \geq 0$ over the whole space, then one assumes

$$\upsilon_{\varphi i} = k_i\sqrt{\Delta_i}, \qquad \sigma_{\varphi i}^2 = \sigma_i^2 + \left(1 - k_i^2\right)\Delta_i, \tag{16}$$

with negative values of k_i describing clockwise rotation. The special case $k_i^2 = 1$ corresponds to the isotropic rotator ($\sigma_{\varphi i} = \sigma_i$), with flattening totally supported by rotation; while, if $k_i = 0$, there is no net rotation ($\upsilon_{\varphi i} = 0$), and the flattening is totally supported by tangential velocity anisotropy. More general velocity decompositions can be obtained by assuming a position-dependent parameter $k_i(R, z)$, also allowing for values greater than unity, up to a position-dependent maximum determined by the request $\sigma_{\varphi i} = 0$ (e.g. Satoh 1980; Ciotti & Pellegrini 1996; Negri, Ciotti & Pellegrini 2014a). In principle each stellar component of a multicomponent model is characterized by a different k_i, so that from equations (16) and (13) the total ρ_* will have an *effective* Satoh parameter k_e given by

$$k_\mathrm{e} \equiv \frac{\upsilon_\varphi}{\sqrt{\Delta}} = \frac{\sum_i k_i\rho_{*i}\sqrt{\Delta_i}}{\rho_*\sqrt{\Delta}}, \quad \sigma_\varphi^2 = \sigma^2 + \left(1 - k_\mathrm{e}^2\right)\Delta, \tag{17}$$

where k_e in general depends on position, even if the k_i do not.

Clearly, in case of $\Delta_i < 0$ for some ρ_{*i}, the Satoh decomposition in equation (16) cannot be applied. The case of a negative Δ_i over some regions of space (or everywhere) is not frequently encountered in applications, but it is not impossible; for example, it necessarily occurs for density components in multicomponent systems with spherically symmetric total density, or in density distributions elongated along the symmetry axis (see e.g. chapter 13 in Ciotti 2021). Indeed, $\Delta = 0$ everywhere for a spherical system supported by a two-integral DF, and thus, from equation (13), at least one Δ_i must be negative (excluding the trivial case of all the subcomponents spherically symmetric, so that $\Delta_i = 0$). Notice that $\Delta_i < 0$ is not necessarily a manifestation of an inconsistent DF ($f_i < 0$), while if $\overline{\mathrm{v}_{\varphi i}^2} = \Delta_i + \sigma_i^2 < 0$ *certainly* the whole model must be discarded as unphysical, even if the solution for the *total* stellar distribution are well behaved. Therefore, if for some component $\Delta_i < 0$, then in case of positivity of the sum $\Delta_i + \sigma_i^2 \geq 0$, the Satoh decomposition is generalized to

$$\upsilon_{\varphi i} = k_i\sqrt{\Delta_i + \sigma_i^2}, \quad \sigma_{\varphi i}^2 = \left(1 - k_i^2\right)\left(\Delta_i + \sigma_i^2\right), \quad k_i^2 \leq 1, \tag{18}$$

where again k_i can depend on position. We refer to this alternative decomposition as to the *generalized* k-decomposition. The case $k_i = 0$ implies no net rotation ($\upsilon_{\varphi i} = 0$), while now $k_i^2 = 1$ corresponds to $\sigma_{\varphi i} = 0$; notice that no isotropic rotators can be realized from equation (18) when $\Delta_i < 0$, because isotropy ($\sigma_{\varphi i} = \sigma_i$) would correspond to $k_i^2 < 0$. Moreover, while with the Satoh decomposition a spherical system cannot rotate and is isotropic independently of the value of k_i, with the generalized k-decomposition one can model rotating (and anisotropic) spherical systems. An application of this last case can be found, for example, in exploratory numerical simulations of rotating gas flows in galaxies of Yoon et al. (2019). Notice that the generalized decomposition applied to systems with $\Delta_i \gg \sigma_i^2$ (as for instance the

case of highly flattened discs) reduces to the standard Satoh formula. A more interesting (and delicate) case, requiring particular care in the choice of the parameter k_i, is represented by systems with $|\Delta_i| \ll \sigma_i^2$, when we have $\upsilon_{\varphi i} \sim k_i \sigma_i$, and $\sigma_{\varphi i}^2 \sim (1-k_i^2)\sigma_i^2$. This means that, in order to avoid substantial rotation, for example in almost spherical systems (oblate or prolate), k_i must be kept small.

We finally remark that, for a given multicomponent system, it is also possible to assume a Satoh decomposition for some components, and the generalized decomposition for the others; in analogy with equation (17) it is possible to define a total *effective* decomposition parameter $k_{\rm e}$ as

$$k_{\rm e} \equiv \frac{\upsilon_\varphi}{\sqrt{\Delta+\sigma^2}}, \quad \sigma_\varphi^2 = \left(1-k_{\rm e}^2\right)\left(\Delta+\sigma^2\right). \tag{19}$$

2.4 Projections

We recast here the projection formulae presented in Posacki et al. (2013) for the case of a multicomponent system, focusing in particular on how the solutions for the components must be summed to obtain the projected fields of the total stellar distribution. We indicate with $\langle\,,\rangle$ the scalar product, with $\boldsymbol{n}$ the line-of-sight direction (hereafter los) directed from the observer to the galaxy,[1] and with l the integration path along the los. For the ease of notation in this Section we drop the subscript i, so that all the following formulae must be intended to hold separately for each stellar component ρ_{*i} (and of course also for the total ρ_*). We will resume the use of the subscript i at the end of the section, when we give the expressions for the projected fields of ρ_* as functions of the projected fields of the components. The projection of a stellar density, and of the ordered velocity $\boldsymbol{\upsilon} = \upsilon_\varphi\, \boldsymbol{e}_\varphi$, are

$$\Sigma_* = \int_{-\infty}^{\infty} \rho_*\, {\rm d}l, \quad \Sigma_* \upsilon_{\rm los} = \int_{-\infty}^{\infty} \rho_* \upsilon_\varphi \langle \boldsymbol{e}_\varphi, \boldsymbol{n}\rangle\, {\rm d}l, \tag{20}$$

where $\boldsymbol{e}_\varphi = (-\sin\varphi, \cos\varphi, 0)$ is the unitary vector in the tangential direction. From the adopted orientation of $\boldsymbol{n}$, a positive/negative $\upsilon_{\rm los}$ indicates a motion receding from/approaching to the observer, respectively. The los velocity dispersion can be written as

$$\sigma_{\rm los}^2 = \sigma_{\rm P}^2 + V_{\rm P}^2 - \upsilon_{\rm los}^2 = V_{\rm rms}^2 - \upsilon_{\rm los}^2 \tag{21}$$

(e.g. Ciotti & Pellegrini 1996; Posacki et al. 2013; CMPZ21), where following Cappellari (2008) we also define $V_{\rm rms}^2 \equiv \sigma_{\rm P}^2 + V_{\rm P}^2$, and

$$\Sigma_* \sigma_{\rm P}^2 = \int_{-\infty}^{\infty} \rho_* \langle \sigma^2 \boldsymbol{n}, \boldsymbol{n}\rangle\, {\rm d}l, \tag{22}$$

$$\Sigma_* V_{\rm P}^2 = \int_{-\infty}^{\infty} \rho_* \upsilon_\varphi^2 \langle \boldsymbol{e}_\varphi, \boldsymbol{n}\rangle^2\, {\rm d}l, \tag{23}$$

where in equation (22) σ is the 3×3 velocity dispersion tensor. The fields $V_{\rm rms}$ and $\upsilon_{\rm los}$ in general depend on the specific direction $\boldsymbol{n}$, and $\upsilon_{\rm los}$, $\sigma_{\rm P}$, and $V_{\rm P}$ on the specific velocity decomposition adopted, but $V_{\rm rms}$ is independent of the velocity decomposition. The previous identities are fully general and hold for a generic inclination of the los with respect to the galaxy. For our axisymmetric models, it is assumed without loss of generality that the los is parallel to the x–z plane, and the projection plane rotates around the y-axis.

In particular, in the face-on projection (hereafter FO), the los is parallel to the z axis with $\boldsymbol{n} = -\boldsymbol{e}_z$, the projection plane is the x–y plane, and

$$\Sigma_* = 2\int_0^{\infty} \rho_*\, {\rm d}z, \quad \Sigma_* \sigma_{\rm los}^2 = 2\int_0^{\infty} \rho_* \sigma^2\, {\rm d}z, \tag{24}$$

because $\upsilon_{\rm los} = V_{\rm P} = 0$, and so $\sigma_{\rm los} = \sigma_{\rm P}$. In the edge-on projection (hereafter EO), the los is aligned with the x-axis with $\boldsymbol{n} = -\boldsymbol{e}_x$, the projection plane coincides with the y–z plane, and $(\cos\varphi, \sin\varphi) = (x/R, y/R)$ where $R = \sqrt{x^2+y^2}$. Then, from equation (20),

$$\Sigma_* = 2\int_y^{\infty} \frac{\rho_* R}{\sqrt{R^2-y^2}}\, {\rm d}R, \quad \Sigma_* \upsilon_{\rm los} = 2y\int_y^{\infty} \frac{\rho_* \upsilon_\varphi}{\sqrt{R^2-y^2}}\, {\rm d}R. \tag{25}$$

Moreover, with some algebra, from equations (22) and (23), we have

$$\Sigma_* \sigma_{\rm P}^2 = 2\int_y^{\infty} \frac{(R^2-y^2)\sigma^2 + y^2\sigma_\varphi^2}{R\sqrt{R^2-y^2}} \rho_*\, {\rm d}R, \tag{26}$$

$$\Sigma_* V_{\rm P}^2 = 2y^2\int_y^{\infty} \frac{\rho_* \upsilon_\varphi^2}{R\sqrt{R^2-y^2}}\, {\rm d}R, \tag{27}$$

so that, from equation (10), equation (21) can be recast in compact form as

$$\Sigma_* \sigma_{\rm los}^2 = 2\int_y^{\infty} \frac{R^2\sigma^2 + y^2\Delta}{R\sqrt{R^2-y^2}} \rho_*\, {\rm d}R - \Sigma_* \upsilon_{\rm los}^2, \tag{28}$$

where the independence of $V_{\rm rms}$ from the specific azimuthal velocity decomposition is apparent.

The projection formulae for a multicomponent stellar system can now be easily obtained, for a generic los, just by considering how the intrinsic quantities add. From equations (1) and (13), and from equations (20)–(23), it is immediate to see that

$$\Sigma_* = \sum_i \Sigma_{*i}, \quad \upsilon_{\rm los} = \frac{\sum_i \Sigma_{*i}\, \upsilon_{{\rm los}i}}{\Sigma_*}, \quad V_{\rm rms}^2 = \frac{\sum_i \Sigma_{*i} V_{{\rm rms}i}^2}{\Sigma_*}, \tag{29}$$

and $\sigma_{\rm los}^2$ is given again by equation (21).

No difficulty is encountered in the construction of the luminosity-weighted fields analogous to equations (29), by using the surface brightness distributions $I_{*i} = \Sigma_{*i}/\Upsilon_{*i}$, and $I_* = \sum_i I_{*i}$, so the *projected* stellar mass-to-light ratio $\Upsilon_{*\rm los} \equiv \Sigma_*/I_*$, defined in analogy with the local Υ_* in equation (4).

Summarizing, we now have the framework needed to determine the solution of the Jeans equations once the solutions for the single components in the total potential are known. In the following section, we detail how the solution of each stellar component is obtained, thanks to the adopted scaling procedure.

3 SCALING OF MULTICOMPONENT MODELS

We show here how, thanks to the full use of the scalings allowed by the Poisson and the Jeans equations, once a set of solutions is obtained for them, one can build an arbitrarily large family of models, just by combining the scaled solutions in this set with different weights; the scheme thus provides several galaxy models with almost no effort. The basic idea is elementary. We recognize that equations (9), at *fixed* total potential Φ, are invariant for a mass scaling of the density ρ_{*i}, i.e. at fixed Φ the derived velocity fields would be independent of the value of M_{*i}. However, as Φ contains also ϕ_{*i}, equations (9) obviously are *not* invariant to such scaling; none the less, the $N+2$

[1] At variance with the convention adopted in CMPZ21, where $\boldsymbol{n}$ points from the galaxy to the observer.

equations for ρ_{*i} in the potentials ϕ_j

$$\begin{cases} \dfrac{\partial \rho_{*i}\sigma_{ij}^2}{\partial z} = -\rho_{*i}\dfrac{\partial \phi_j}{\partial z}, \\ \dfrac{\partial \rho_{*i}\sigma_{ij}^2}{\partial R} = \rho_{*i}\dfrac{\Delta_{ij}}{R} - \rho_{*i}\dfrac{\partial \phi_j}{\partial R}, \end{cases} \tag{30}$$

and their solutions

$$\rho_{*i}\sigma_{ij}^2 = \int_z^\infty \rho_{*i}\frac{\partial \phi_j}{\partial z'}\,\mathrm{d}z', \quad \rho_{*i}\Delta_{ij} = R\left(\frac{\partial \rho_{*i}\sigma_{ij}^2}{\partial R} + \rho_{*i}\frac{\partial \phi_j}{\partial R}\right), \tag{31}$$

with $\rho_{*i}\sigma_{ij}^2 \to 0$ for $z \to \infty$, do have important scaling properties that will be exploited in Section 3.1. We note that here and in the following the double subscript in σ_{ij}^2 does not refer to the tensorial nature of the velocity dispersion, but just identifies the solution of the i-th stellar component in the j-th potential component.

Leaving aside for the moment the scaling properties of equations (30) and (31), it is obvious that the sums

$$\sigma_i^2 = \sum_j \sigma_{ij}^2, \quad \Delta_i = \sum_j \Delta_{ij}, \tag{32}$$

are the solution of equations (9), as can be demonstrated, first by summing over j the $N+2$ equations (30) and their solutions (31), and comparing the resulting expressions with equations (9) and (11), and then by proving that the solution of equation (9) is unique from the imposed boundaries.

An important point is in order here. Despite the apparent similarity of the decomposition of σ_i^2 and Δ_i performed in equations (30) over the $N+2$ potential components ϕ_j, with the decomposition of σ^2 and Δ performed in equations (9) over the N stellar components ρ_{*i}, there is a fundamental conceptual difference between the two decompositions. In fact, equations (9) are *true* moments of the collisionless Boltzmann equation obeyed by the distribution functions f_i in the total potential, and so they have a sort of autonomous physical meaning; equations (30), instead, are just a mathematical decomposition over the different ϕ_j of the Jeans equations for ρ_{*i}. As a consequence, phase-space consistency arguments apply to the solution of equations (9), but not to σ_{ij}^2 and Δ_{ij} separately: as far as the fields σ_i^2 and Δ_i are physically acceptable, the model is also acceptable, independently of the specific properties[2] of its components σ_{ij}^2 and Δ_{ij}.

Finally, we recall the decomposition rule for the Virial Theorem (in its scalar form; the formulae can be easily extended to its tensorial form) of each stellar component:

$$2K_{*i} = -W_i = -\sum_j W_{ij}, \tag{33}$$

where K_{*i} is the kinetic energy of the i-th stellar component, and

$$W_{ij} = -4\pi G\int_0^\infty\int_0^\infty \rho_{*i}\left(R\frac{\partial \phi_j}{\partial R} + z\frac{\partial \phi_j}{\partial z}\right)R\,\mathrm{d}R\,\mathrm{d}z. \tag{34}$$

3.1 The scaling scheme

We describe below how the scaling scheme works in general, with particular reference to its numerical implementation in JASMINE2, and to its logically distinct parts of the Potential and Jeans Solver and of the PP. We distinguish three groups of model parameters for the construction of a multicomponent model, summarized in Table 1. In the first group there are the *physical scales* M_* and r_*, i.e. the total stellar mass and its scale length. All the density and potential components are made dimensionless by scaling them to the quantities

$$\rho_\mathrm{n} \equiv \frac{M_*}{4\pi r_*^3}, \quad \phi_\mathrm{n} \equiv \frac{GM_*}{r_*}. \tag{35}$$

We note that it is convenient to normalize the 2D numerical grid to r_*, with $\tilde{R} \equiv R/r_*$ and $\tilde{z} \equiv z/r_*$. A scaled grid guarantees the same resolution, independently of the actual physical size of the model, measured by r_*. Incidentally, JASMINE2 has a bilogarithmic grid, with a few hundreds of points in $\tilde{R}$ and $\tilde{z}$, ranging from $\approx 10^{-5}$ or less at the origin, up to $\approx 10^2$ or more at the outer edge. *Even though the physical scales are logically introduced first, the values of M_* and r_* (and so of ρ_n and ϕ_n) are fixed in the last step of the model construction, at the end of the PP (see Table 1).* In this way, different physical realizations (in size and total mass) can be obtained for the same multicomponent galaxy model.

In the second group of parameters, there are the relative mass weights $\mathcal{R}_i \equiv M_{*i}/M_*$, $\mathcal{R}_\mathrm{h} \equiv M_\mathrm{h}/M_*$, $\mathcal{R}_\mathrm{BH} \equiv M_\mathrm{BH}/M_*$ of the different components, the mass-to-light ratios Υ_{*i}, and the parameters k_i appearing in equations (16) and (18) for the kinematical decomposition of the azimuthal motions. By definition

$$\sum_i \mathcal{R}_i = 1, \tag{36}$$

and in full generality we write

$$\rho_{*i} = \rho_\mathrm{n}\mathcal{R}_i\tilde{\rho}_{*i}, \quad \rho_\mathrm{h} = \rho_\mathrm{n}\mathcal{R}_\mathrm{h}\tilde{\rho}_\mathrm{h}, \quad \tilde{\rho}_* = \sum_i \mathcal{R}_i\tilde{\rho}_{*i}. \tag{37}$$

where $\tilde{\rho}_{*i}$ and $\tilde{\rho}_\mathrm{h}$ are the *scaled* density distributions, and $\tilde{\rho}_* = \rho_*/\rho_\mathrm{n}$ is the dimensionless total stellar density. Notice that from equation (35) the volume integrals of $\tilde{\rho}_{*i}$ over the whole dimensionless numerical grid evaluate to 4π by construction. Similarly,

$$\phi_{*i} = \phi_\mathrm{n}\mathcal{R}_i\tilde{\phi}_{*i}, \ \phi_\mathrm{h} = \phi_\mathrm{n}\mathcal{R}_\mathrm{h}\tilde{\phi}_\mathrm{h}, \ \phi_\mathrm{BH} = \phi_\mathrm{n}\mathcal{R}_\mathrm{BH}\tilde{\phi}_\mathrm{BH}, \tag{38}$$

Table 1. The three main steps involved in the construction of a multicomponent model, listed from top to bottom in the order in which they are considered in a numerical implementation of the scaling scheme (as described in Section 3.1).

Parameters of the scaling scheme	
Potential and Jeans Solver	
Structural parameters	
Scaled stellar and DM densities	$\tilde{\rho}_{*i}$, $\tilde{\rho}_\mathrm{h}$
Scale-length ratios	$\xi_i = \dfrac{r_{*i}}{r_*}$, $\xi_\mathrm{h} = \dfrac{r_\mathrm{h}}{r_*}, \ldots$
Shape parameters	$q_i, q_\mathrm{h}, \ldots$
Post-processing	
Weights	
Mass ratios	$\mathcal{R}_i = \dfrac{M_{*i}}{M_*}$, $\mathcal{R}_\mathrm{h} = \dfrac{M_\mathrm{h}}{M_*}$, $\mathcal{R}_\mathrm{BH} = \dfrac{M_\mathrm{BH}}{M_*}$
Mass-to-light ratios	$\Upsilon_{*i} = \dfrac{M_{*i}}{L_i}$
Kinematical decompositions	k_i, λ_i, δ_i
Post-processing	
Physical scales	
Total stellar mass	M_*
Total stellar density scale length	r_*

[2]The situation is somewhat similar to that faced when decomposing a positive density distribution over some prescribed set of functions (e.g. spherical harmonics), when the basis functions can present regions of negative densities.

and so

$$\Phi = \phi_{\rm n} \sum_j \mathcal{R}_j \tilde{\phi}_j, \quad W_i = M_* \phi_{\rm n} \mathcal{R}_i \sum_j \mathcal{R}_j \tilde{W}_{ij}, \tag{39}$$

and

$$\sigma_i^2 = \phi_{\rm n} \tilde{\sigma}_i^2 = \phi_{\rm n} \sum_j \mathcal{R}_j \tilde{\sigma}_{ij}^2, \quad \Delta_i = \phi_{\rm n} \tilde{\Delta}_i = \phi_{\rm n} \sum_j \mathcal{R}_j \tilde{\Delta}_{ij}. \tag{40}$$

Finally, from the assumption of a constant mass-to-light ratio Υ_{*i} for each stellar component,

$$\nu_{*i} = \rho_{\rm n} \frac{\mathcal{R}_i}{\Upsilon_{*i}} \tilde{\rho}_{*i}, \quad L_i = \frac{\mathcal{R}_i}{\Upsilon_{*i}} M_*. \tag{41}$$

The values of the weights are chosen in PP (see Table 1), because a change in their values, and in the kinematical decompositions, does not require to recompute the potentials and solve again the Jeans equations. This possibility allows for a fast construction of different models belonging to the same family.

One family indeed is characterized by the choice of the third group of parameters, to be performed at the beginning of the model construction: the *structural parameters* of the scaled density components $\tilde{\rho}_{*i}$ and $\tilde{\rho}_{\rm h}$, that in full generality we indicate with the symbols $\xi_i \equiv r_{*i}/r_*$ and $\xi_{\rm h} \equiv r_{\rm h}/r_*$ for the different scale lengths, and with q_i and $q_{\rm h}$ for other parameters that determine the shape of the scaled densities (for example the flattenings in case of ellipsoidal density distributions). *The values of the structural parameters must be assigned in order to run the Potential and Jeans Solver (see Table 1), and in general a change in some of their values requires a new computation of the potentials and of the Jeans solutions.*

3.1.1 The Potential and Jeans Solver

For a chosen set of values for the structural parameters, the scaled Jeans equations are obtained from equations (30) and equations (37) and (38). In practice, for N assigned scaled stellar components $\tilde{\rho}_{*i}$ and a scaled dark matter halo $\tilde{\rho}_{\rm h}$, the Potential and Jeans Solver first computes the scaled potentials $\tilde{\phi}_{*i}$ and $\tilde{\phi}_{\rm h}$, and then solves the $N \times (N + 2)$ pairs of scaled equations (30), one for each $\tilde{\rho}_{*i}$ in the potential $\tilde{\phi}_j$ (including $\tilde{\phi}_{\rm BH}$), over the dimensionless grid $(\tilde{R}, \tilde{z})$; thus, the scaled fields $\tilde{\sigma}_{ij}^2$ and $\tilde{\Delta}_{ij}$ are obtained. The possibility to solve equations (30) without choosing $\mathcal{R}_i$ and $\mathcal{R}_j$ is due to the fact that, on one hand, the weights $\mathcal{R}_i$ appear linearly in both sides of equations (30); on the other hand, $\tilde{\sigma}_{ij}^2$ and $\tilde{\Delta}_{ij}$ scale linearly with $\mathcal{R}_j$, once the boundary condition is fixed to zero at infinity.

The details of the numerical implementation of the computation of the potentials and of the solution of the Jeans equations are described in Posacki et al. (2013). Here, we recall that the standard choice for the numerical computation of the potential in JASMINE2 is the integral formula

$$\phi = -4G \int_0^\infty R' \, {\rm d}R' \int_{-\infty}^\infty \frac{\rho(R', z') \, {\rm d}z'}{\sqrt{(R + R')^2 + \Delta z^2}} \boldsymbol{K} \left[\sqrt{\frac{4RR'}{(R + R')^2 + \Delta z^2}} \right], \tag{42}$$

where $\Delta z = z - z'$, and $\boldsymbol{K}$ is the complete elliptic integral of the first kind (see e.g. BT08; Ciotti 2021), evaluated as a two-dimensional integration over a staggered grid. However, for genuinely ellipsoidal models, the code can the use the faster Chandrasekhar formula (e.g. equation 2.140 in BT08; equation 2.21 in Ciotti 2021), and, for disc distributions, the integral formula based on Bessel functions (see Section 4.3 and Appendix B). As already remarked, the numerical evaluation of the potential is the most time consuming part of the construction of a model. For this reason, JASMINE2 also contains a continuously updated library of analytical density-potential pairs available in the literature (and in some cases also based on homoeoidal expansion, see e.g. Ciotti & Bertin 2005), so that one can choose between the numerical computation of the potential and (when available) the use of the analytical potential.

3.1.2 The post-processing

As described in the previous section, for a given multicomponent model of assigned $\tilde{\rho}_{*i}$, $\tilde{\rho}_{\rm h}$, and with a central BH, the Potential and Jeans Solver gives the solution $\tilde{\sigma}_{ij}^2$ and $\tilde{\Delta}_{ij}$ of the scaled form of equations (30). These solutions are then combined in PP, with the assignment of the mass ratios $\mathcal{R}_j$, so that the solution σ_i^2 and Δ_i of equations (9) for ρ_{*i} is obtained, according to equations (32) and (40). At this stage, as discussed in Section 2.3, the PP performs a positivity check of $\tilde{\Delta}_i$ and $\tilde{\Delta}_i + \tilde{\sigma}_i^2$: in case of negativity of the last quantity, a new choice of the weights $\mathcal{R}_j$ is made, until positivity is reached. If positivity cannot be obtained for acceptable choices of $\mathcal{R}_j$, then the multicomponent model is discarded as unphysical.

Once the mass weights are assigned and the positivity check is passed, the PP requires the parameter k_i for the kinematical decomposition, that gives the scaled azimuthal velocity fields $\upsilon_{\varphi i}$ and $\sigma_{\varphi i}$. In full generality, we define each decomposition parameter as

$$k_i(R, z) = \lambda_i \delta_i(R, z), \tag{43}$$

where λ_i is a constant weight, and $\delta_i(R, z)$ is a position-dependent function; the standard Satoh parameter is obtained with $\delta_i = 1$ and $\lambda_i = k_i$. The benefit of this factorization is due to the fact that the projection formula of $\upsilon_{\varphi i}$ in equation (20) for a given $\delta_i(R, z)$ scales with λ_i, so that we can set the value of λ_i *after* having computed the projection integral. As projections represent the second most time-consuming step, the possibility to choose (and change) λ_i after projections is a significant advantage. Note that, at variance with what happens for the fields $\tilde{\sigma}_i^2$, $\tilde{\Delta}_i$, $\tilde{\upsilon}_{\varphi i}^2$, and $\tilde{\sigma}_{\varphi i}^2$, the mass weights $\mathcal{R}_j$ enter the expression of $\tilde{\upsilon}_{\varphi i}$ under a square root (see equations 16 and 18). This implies that the $\mathcal{R}_j$ must be chosen before calculating the projections that use $\upsilon_{\varphi i}$.[3] In other words, the possibility to modify the values of $\mathcal{R}_j$ in PP, allowed by the '*ij*-decomposition', ends with the computation of the scaled fields in equations (40).

Once we have obtained the intrinsic and projected fields of each ρ_{*i}, the last steps are to combine them to calculate the *total* (mass- and luminosity-weighted) intrinsic and projected fields of ρ_* (respectively from equations 13 and 14, and equations 20, 21, and 29), and finally to choose the physical scales M_* and r_*.

3.2 Summary

Summarizing, a *family* of multicomponent galaxy models is defined by the choice of N scaled stellar density components $\tilde{\rho}_{*i}$, a scaled DM halo $\tilde{\rho}_{\rm h}$, and a central BH. The Potential and Jeans Solver computes the associated scaled potentials $\tilde{\phi}_j$, and then solves the $N \times (N + 2)$ Jeans equations (30) in their scaled form. In the subsequent PP, specific values of the mass ratios $\mathcal{R}_i$, $\mathcal{R}_{\rm h}$, $\mathcal{R}_{\rm BH}$, of the mass-to-light ratios Υ_{*i}, and of the kinematical decompositions with the parameters k_i, are fixed, thus defining a specific model in the same

[3]The *effective radius* $R_{\rm e}$ of the total stellar distribution is obviously another important quantity that cannot be obtained as a linear combination of the effective radii of the stellar components, and it can only be computed after the choice of the weights $\mathcal{R}_i$ and Υ_{*i}.

family. The solution of the Jeans equations for the total density distribution is recovered as (mass- or luminosity-) weighted sums of the scaled solutions, and the projections along a given line-of-sight are performed. The values of the total stellar mass M_*, and of its scale length r_*, complete the construction of the model.

There are at least two significant advantages in this procedure, when compared with a straightforward integration of the Jeans equations for a multicomponent galaxy model. First, the gravitational potentials of each stellar component and of the DM halo need not to be recalculated every time the weights are changed in PP; thus, the run of the most time expensive part of is required just once for all the models in the same family. Secondly, the possibility to choose the weight parameters in PP allows for a fast exploration of the parameter space (that, for multicomponent models, can be very large). Qualitatively, the $N \times (N+2)$ set of the ij-th scaled solutions of the Jeans equations for each i-th density component in each j-th potential component, can be interpreted as *basis vectors* that are successively linearly combined with different weights, to obtain a specific solution belonging to a family of multicomponent models.

As a final remark, note that the procedure described so far can be extended to more general velocity decompositions. For example, it is straightforward to insert in it the Cappellari (2008) orbital anisotropy, where $\sigma_{Ri} = b_i\,\sigma_{zi}$, with b_i a constant parameter that can be different for each stellar component, and the underlying i-th DF depends on three integrals of motion.

4 FOUR ILLUSTRATIVE MULTICOMPONENT MODELS

In order to illustrate the new features and potentialities of our procedure, as implemented in JASMINE2, we first describe in some detail the building of three multicomponent galaxy models. All three models are made of two stellar distributions, to which a DM halo with a spherical Navarro–Frenk–White profile (Navarro, Frenk & White 1996, hereafter NFW) and a central supermassive BH are added. In the first model (hereafter JJE), the *total* spherical stellar profile and an ellipsoidal stellar component, both with a Jaffe (1983) profile, are assigned; if the dark mass is set to zero, this model reduces to the JJe models of CMPZ21. The second model (hereafter JHD) consists of an ellipsoidal Jaffe stellar density distribution, that represents a light stellar halo, coupled with a heavy Miyamoto–Nagai stellar disc (hereafter MN, Miyamoto & Nagai 1975). In the third model (hereafter JLD), the ellipsoidal Jaffe component dominates, while a small MN inner disc is counter-rotating. These three models are intended to represent features observed in real galaxies, but they are not designed to reproduce specific objects. Finally, we illustrate the comparison between an exponential disc and its representation via the sum of three MN discs, as proposed by Smith et al. (2015).

4.1 The JJE models

JJE models are a natural generalization of JJe models presented in CMPZ21: as these latter describe quite well real elliptical galaxies, and several of their dynamical properties can be expressed in analytical form, they also represent an obvious test for JASMINE2.

To better appreciate the properties of JJE models, we recall the main properties (and limitations) of JJe models. These are constructed by assigning a *total* density ρ_* following the axisymmetric ellipsoidal generalization of the Jaffe model, and another axisymmetric ellipsoidal Jaffe distribution ρ_{*1}, with different flattening, scale length, and total mass; in CMPZ21 the density distribution $\rho_* - \rho_{*1}$ ($=\rho_{*2}$ in the current notation), is interpreted as a DM halo; finally, a central BH is added to the system. The analytical conditions on ρ_{*1} to guarantee the positivity of ρ_{*2} are given, and then the Jeans equations for ρ_{*1} are solved in analytical closed form, by using homoeoidal expansion, truncated at the linear order in the flattenings of ρ_* and ρ_{*1}. Albeit several properties of JJe models can be expressed in analytical form (making these models quite useful in numerical simulations of gas flows in galaxies, see e.g. Gan et al. 2019a, b), a few important shortcomings still affect them: (i) the Jeans equations for ρ_{*1} are integrated in the homoeoidal expansion limit, retaining only linear terms in the flattenings, and they have not been studied for the difference component ρ_{*2}; (ii) projected kinematical fields of ρ_{*1} can be obtained in analytical form only as asymptotic formulae at the centre and at large radii. JASMINE2 is then the obvious tool to address the two points above.

Here, we generalize the JJe models to JJE models, by considering for the total ρ_* an ellipsoidal Jaffe profile, of total mass M_*, scale length[4] ξ, and flattening q:

$$\rho_*(R,z) = \frac{\rho_{\rm n}\xi}{q\,m^2(\xi+m)^2}, \quad m^2 = \tilde{R}^2 + \frac{\tilde{z}^2}{q^2}. \tag{44}$$

Therefore, at variance with JJe models, in JJE models the total Jaffe mass distribution is purely stellar. We then consider another ellipsoidal Jaffe density profile, of total mass $M_{*1} = \mathcal{R}_1 M_*$, scale-length $r_{*1} = \xi_1 r_*$, and flattening q_1:

$$\rho_{*1}(R,z) = \frac{\rho_{\rm n}\mathcal{R}_1\xi_1}{q_1 m_1^2(\xi_1+m_1)^2}, \quad m_1^2 = \tilde{R}^2 + \frac{\tilde{z}^2}{q_1^2}. \tag{45}$$

The second stellar component is then defined as

$$\rho_{*2}(R,z) = \rho_*(R,z) - \rho_{*1}(R,z), \tag{46}$$

with $M_{*2} = M_* - M_{*1} = (1-\mathcal{R}_1)\,M_* = \mathcal{R}_2\,M_*$, in agreement with equation (36). Notice that ρ_{*2} is not an ellipsoid, unless $q_1 = q$, and even in this case ρ_{*2} is not a Jaffe ellipsoid, unless $\xi_1 = \xi$. As extensively discussed in CMPZ21, ρ_{*2} could be negative somewhere (and so unphysical) for some choices of $\mathcal{R}_1$, ξ_1, and q_1. Remarkably, the conditions required to assure $\rho_{*2} \geq 0$ can be expressed as analytical (and simple) inequalities, as shown in Appendix A.

The stellar distribution ρ_* is embedded in an NFW DM halo (spherically symmetric for simplicity), of mass $M_{\rm h}(r_{\rm t}) = \mathcal{R}_{\rm h} M_*$ enclosed within a truncation radius $r_{\rm t}$, scale length $r_{\rm h} = \xi_{\rm h} r_*$, and concentration $c \equiv r_{\rm t}/r_{\rm h}$:

$$\rho_{\rm h}(r) = \frac{\rho_{\rm n}\mathcal{R}_{\rm h}}{f(c)s(\xi_{\rm h}+s)^2}, \quad \phi_{\rm h}(r) = -\phi_{\rm n}\mathcal{R}_{\rm h}\frac{\ln(1+s/\xi_{\rm h})}{f(c)s}, \tag{47}$$

where $s \equiv r/r_*$ and $f(c) = \ln(1+c) - c/(1+c)$. We complete the model with a central BH of mass $M_{\rm BH} = \mathcal{R}_{\rm BH} M_*$.

Summarizing, JJE models are determined, besides the total stellar mass and scale length, M_* and r_*, by the two parameters ξ and q for ρ_*, the five parameters q_1, ξ_1, $\mathcal{R}_1$, Υ_{*1}, k_1, for ρ_{*1}, the two parameters Υ_{*2}, k_2 for ρ_{*2}, the three DM parameters $\xi_{\rm h}$, c, $\mathcal{R}_{\rm h}$, and the BH mass weight $\mathcal{R}_{\rm BH}$ (see Table 2 for a specific JJE model). JASMINE2 further generalizes JJE models, with the addition of a second DM component given by a shallow and very extended quasi-isothermal halo, as useful in simulations of gas flows in galaxies residing in groups or clusters (Ciotti et al. in preparation).

[4]In the spherical limit, and in the assumption of constant mass-to-light ratio, the Jaffe scale radius r_* is related to the effective radius by $R_{\rm e} \simeq 0.75\,r_*$.

Table 2. The parameters for the stellar components of the illustrative JJE, JHD and JLD models (Sections 4.1 and 4.2). In the JJE model, the component ρ_{*2} is obtained as *difference* between a total spherical ($q = 1$) Jaffe profile ρ_*, with scale length $\xi = 1$, and a small and light Jaffe ellipsoidal component ρ_{*1} (as done for JJe models in CMPZ21). The standard Satoh k-decomposition in equation (16) for ρ_{*1}, and the generalized k-decomposition in equation (18) for ρ_{*2}, are adopted. In the JHD model, an ellipsoidal Jaffe distribution is coupled to a massive and quite flat ($q_2 = a/b = 10$) MN disc; in both components a generalized k-decomposition is adopted. In the JLD model, the ellipsoidal Jaffe component has the same flattening and size as in the JHD model, but the disc is significantly smaller, and counter-rotates in the inner regions, with the position-dependent Satoh parameter in equation (50), while a constant Satoh parameter is applied to the Jaffe component. In all models, the DM halo has a spherical NFW profile with $\xi_\mathrm{h} = 2.6$, $c = 10$, $\mathcal{R}_\mathrm{h} = 20$, and the BH is defined by $\mathcal{R}_\mathrm{BH} = 0.002$.

Model	ρ_{*1}	ρ_{*2}
JJE	Jaffe	$\rho_*(\xi = 1, q = 1) - \rho_{*1}$
	$\xi_1 = 0.1$	–
	$q_1 = 0.8$	–
	$\mathcal{R}_1 = 0.04$	$\mathcal{R}_2 = 0.96$
	$\Upsilon_{*1} = 2$	$\Upsilon_{*2} = 6$
	$k_1 = 0.5$	$k_2 = 0.2$
JHD	Jaffe	MN
	$\xi_1 = 1$	$\tilde{b} = 0.1$
	$q_1 = 0.8$	$q_2 = 10$
	$\mathcal{R}_1 = 0.3$	$\mathcal{R}_2 = 0.7$
	$\Upsilon_{*1} = 6$	$\Upsilon_{*2} = 2$
	$k_1 = 0.5$	$k_2 = 0.8$
JLD	Jaffe	MN
	$\xi_1 = 1$	$\tilde{b} = 0.01$
	$q_1 = 0.8$	$q_2 = 10$
	$\mathcal{R}_1 = 0.96$	$\mathcal{R}_2 = 0.04$
	$\Upsilon_{*1} = 6$	$\Upsilon_{*2} = 2$
	$k_1 = 0.5$	$k_2(R, z)$

4.1.1 Tests

We can use JASMINE2 in two different tests: we can give in input the homoeoidal expansion of the density-potential pairs, truncated at the linear order, and compare the numerical solution with that of CMPZ21, to check the importance of quadratic flattening terms in the solution of the Jeans equations for JJe models; and we can give in input the *true* ellipsoidal model, to check how well the homoeoidal expansion reproduces its internal dynamics. At the same time, the previous tests allow for an accuracy check of JASMINE2.

In the first test, we feed JASMINE2 with the homoeoidal expansion for ρ_* and ρ_{*1}, and we compare the numerical results of integration of the Jeans equations with the analytical results: we obtain excellent agreement for all the kinematical fields, better than a fraction of per cent over the whole numerical grid, ranging from $\approx 10^{-5}$ to ≈ 70 (in units of r_*). The results tend to be slightly more discrepant at increasing flattenings, as expected, since the analytical results in CMPZ21 are limited to the *linear* order in the flattenings, while JASMINE2 takes automatically into account also the *second*-order terms when integrating the Jeans equations (due to the product between the density and the gradient of the potential). By increasing the numerical resolution in the central regions, and moving to smaller and smaller distances from the centre, we also verify that the asymptotic formulae for the projected kinematical fields are also perfectly recovered numerically. This first test adds confidence that JASMINE2 is working properly and with high accuracy, but also provides a further support that the (quite cumbersome) analytical formulae in CMPZ21 are actually correct.[5]

In a second test, we compare the numerical results of JASMINE2 for the *true* ellipsoidal JJe models with the analytical results in CMPZ21 obtained from homoeoidal expansion, therefore moving beyond the effect of second order approximation in the flattenings explored in the first test. We find that for relatively small flattenings (corresponding to E2–E3 galaxies) the homoeoidal expansion truncated at the linear order provides quite good results, even when compared with true ellipsoidal models, with the most significant discrepancy in the intermediate regions.

4.1.2 Results for a JJE model

We move now to illustrate the main properties of a specific JJE model (see Table 2). The total stellar distribution ρ_* has a spherical Jaffe profile obtained from equation (44) with $\xi = 1$ and $q = 1$; this quite artificial case allows us to discuss some subtleties that can occur to the kinematical decomposition in multicomponent systems. The stellar component ρ_{*1} is obtained from equation (45) with $\xi_1 = 0.1$, $q_1 = 0.8$, $\mathcal{R}_1$ is 0.04, and $\Upsilon_{*1} = 2$, i.e. it is a quite small ellipsoidal distribution at the centre of the galaxy; note that, from equation (A15), the maximum possible value of $\mathcal{R}_1$ is 0.08. The component ρ_{*2} accounts for the remaining 96 per cent of the total stellar mass of the galaxy, and $\Upsilon_{*2} = 6$, so that ρ_* could represent an elliptical galaxy with a central and younger stellar system. We add the spherical NFW DM halo, given by equation (47), with $\xi_\mathrm{h} = 2.6$, $c = 10$, and $\mathcal{R}_\mathrm{h} = 20$, so that the DM mass inside R_e (see Footnote 3) is $\approx$0.45 of the total mass. Finally, in agreement with BH–galaxy scaling relations (see e.g. Kormendy & Ho 2013), the mass of the central BH is fixed to $\mathcal{R}_\mathrm{BH} = 0.002$.

In the three top panels of Fig. 1, we show the density distribution of the scaled components $\tilde{\rho}_{*1}$ and $\tilde{\rho}_{*2}$, and of the total stellar density $\tilde{\rho}_* = \rho_*/\rho_\mathrm{n}$. Being this last spherical, and $\tilde{\rho}_{*1}$ oblate, $\tilde{\rho}_{*2}$ in its central regions is slightly prolate, and this will affect its kinematical fields, as anticipated in Section 2.3. Additional information on the model structure is provided in the first column of Fig. 2: the top panel shows the radial profiles in the equatorial plane of $\mathcal{R}_1\tilde{\rho}_{*1}$, $\mathcal{R}_2\tilde{\rho}_{*2}$, $\tilde{\rho}_*$, and $\mathcal{R}_\mathrm{h}\tilde{\rho}_\mathrm{h}$. The total ρ_* is almost coincident with ρ_{*2}, except for the central regions, where ρ_{*1} and ρ_{*2} are comparable. The DM density ρ_h overcomes ρ_* outside $\approx 0.5\ R_\mathrm{e}$. The bottom panel shows the radial profiles in the equatorial plane of the contributions to the circular velocity due to the various mass components: the BH contribution is dominant in the inner regions, the DM in the outer regions, while at intermediate distances from the centre the resulting circular velocity is quite flat.

Similar trends can be seen in the radial profiles of the velocity fields in the equatorial plane of Fig. 3, where, in the first column from top to bottom, we show the rotational velocity, the vertical velocity dispersion, and the azimuthal velocity dispersion, of ρ_{*1} and ρ_{*2}, and the total mass-weighted and luminosity-weighted fields. Note that in the three panels the vertical scale is the same, and the resulting system is clearly a slow rotator. This JJE model offers the opportunity to apply the generalized k-decomposition in equation (18); because the field Δ_2, associated with the slightly prolate ρ_{*2},

[5]These tests are similar in the approach to those already performed with JASMINE by using the analytical results of Smet, Posacki & Ciotti (2015): we recall that the numerical integration of the potential in JASMINE2 uses the same routines of JASMINE.

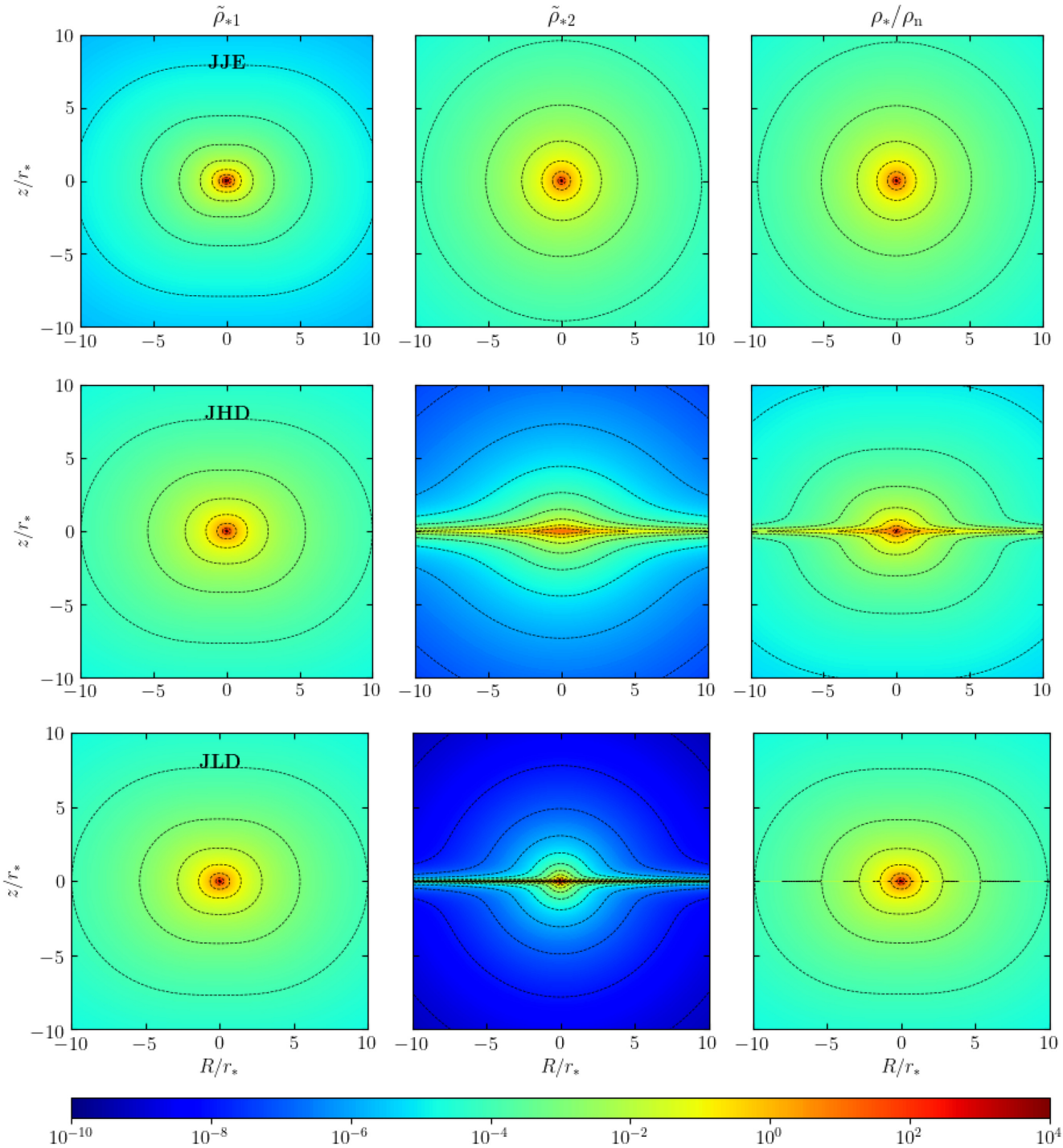

Figure 1. The scaled stellar distributions $\tilde{\rho}_{*1}$, $\tilde{\rho}_{*2}$, and the dimensionless total stellar distribution $\tilde{\rho}_* = \rho_*/\rho_n$, of the three models of Table 2. The dotted contours show the isodensities, with values spaced by 1 dex.

is negative in the central regions. As discussed in Section 2.3, we verified that $\overline{v_{\varphi 2}^2}$ is nowhere negative, and then we adopted the generalized decomposition, with a quite small $k_2 = 0.2$. The field Δ_1 instead is everywhere positive, as expected, and so we adopted the standard Satoh formula with $k_1 = 0.5$. In the velocity profiles, the effect of the central BH is clearly visible; for example, the velocity dispersion profile of a Jaffe model with $\mathcal{R}_{BH} = 0$ would be constant in the central regions. Notice also how the velocity profiles, outside $\approx R_e$, are almost coincident with the profiles of the more massive component ρ_{*2}, in both the mass-weighted and luminosity-weighted cases; this is not surprising, because in these regions ρ_* coincides with ρ_{*2} (see Figs 1 and 2). The situation is different in the inner regions, where ρ_{*1} and ρ_{*2} are comparable: here the total velocities have intermediate values, with the luminosity-weighted profiles closer to the profiles of ρ_{*1} with the smaller mass-to-light ratio.

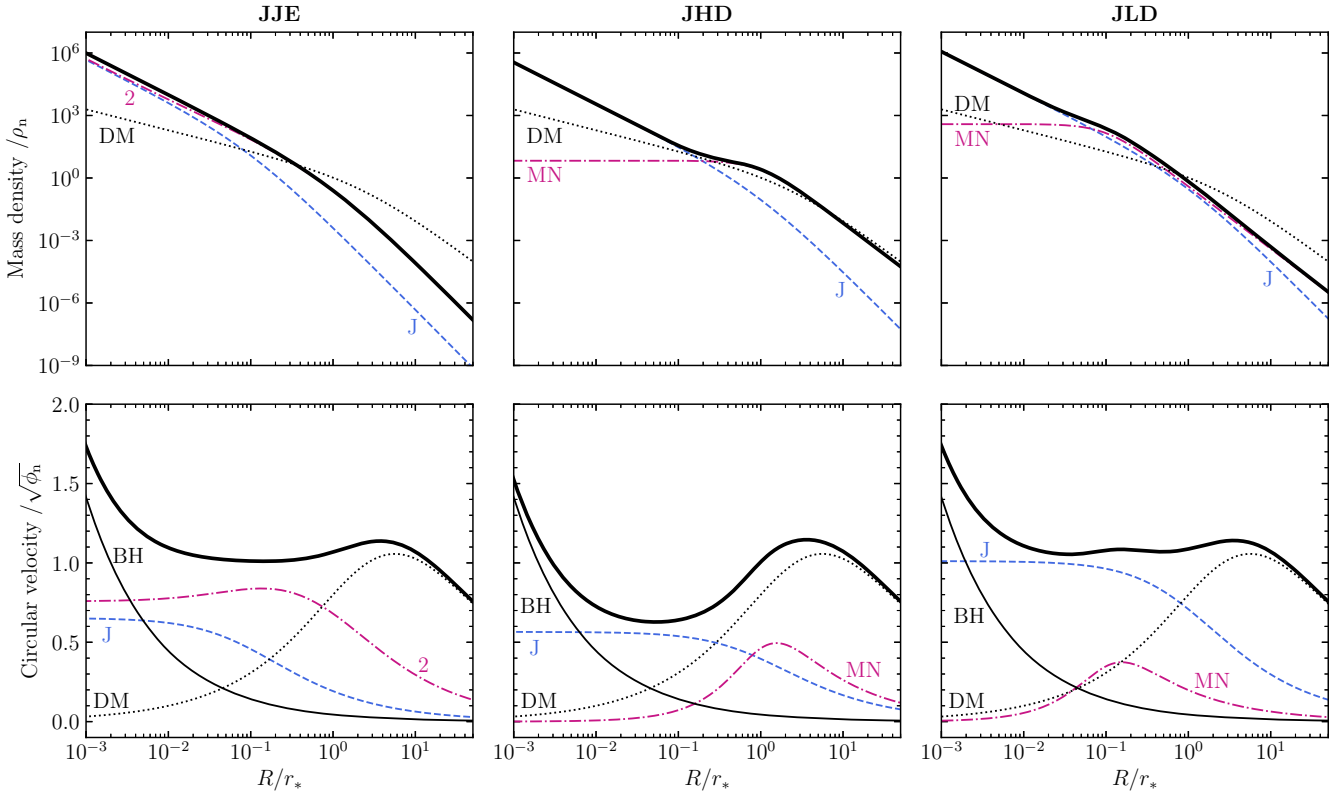

Figure 2. Radial profiles in the equatorial plane ($\tilde{z} = 0$) of the mass densities $\mathcal{R}_1\tilde{\rho}_{*1}$ (dashed blue), $\mathcal{R}_2\tilde{\rho}_{*2}$ (dot–dashed magenta), $\tilde{\rho}_*$ (heavy solid), and $\mathcal{R}_h\tilde{\rho}_h$ (dotted), normalized to ρ_n (top row), for the three models of Table 2. In the bottom row, we show the corresponding contributions to the total circular velocity (heavy solid) in the equatorial plane of the mass components, with the additional contribution of the central BH (solid), all normalized to $\sqrt{\phi_n}$.

As an illustration of the projection procedure, in the first row of Fig. 4, we show the EO projected luminosity-weighted fields $\upsilon_{\mathrm{los}\mathscr{L}}$ and $\sigma_{\mathrm{los}\mathscr{L}}$, with the superimposed dotted contours representing the galaxy isophotes of the surface brightness I_*. The slow rotation of the model is apparent from the colourbar values, indeed $\upsilon_{\mathrm{los}\mathscr{L}}$ is everywhere lower than $\sigma_{\mathrm{los}\mathscr{L}}$. A curious feature is the slightly vertically elongated shape of $\sigma_{\mathrm{los}\mathscr{L}}$: this is *not* due to the prolate shape of ρ_{*2} in the central regions, but it is an effect of the generalized k-decomposition, coupled with the fact that Δ_2 is almost null in the external regions, and so here $\upsilon_{\varphi 2} \sim k_2\sigma_2$, as introduced in Section 2.3. For example, an increase in k_2 would lead to an increase of the rotation in the external regions, with correspondent decrease of $\sigma_{\mathrm{los}\mathscr{L}}$, and with the net result of a more elongation of $\sigma_{\mathrm{los}\mathscr{L}}$ in the central regions.

4.2 Ellipsoidal models with an embedded stellar disc

JHD and JLD models consist of a stellar profile ρ_{*1} given again by the ellipsoidal Jaffe model in equation (45), coupled with a stellar MN disc ρ_{*2}, of total mass $M_{*2} = \mathcal{R}_2 M_*$, and scale lengths $a = \tilde{a}r_*$, $b = \tilde{b}r_*$:

$$\rho_{*2}(R, z) = \rho_n \mathcal{R}_2 \tilde{b}^2 \frac{\tilde{a}\tilde{R}^2 + (\zeta + 2\sqrt{\tilde{z}^2 + \tilde{b}^2})\zeta^2}{(\tilde{R}^2 + \zeta^2)^{5/2}(\tilde{z}^2 + \tilde{b}^2)^{3/2}}, \tag{48}$$

$$\phi_{*2}(R, z) = -\frac{\phi_n \mathcal{R}_2}{\sqrt{\tilde{R}^2 + \zeta^2}}, \quad \zeta = \tilde{a} + \sqrt{\tilde{z}^2 + \tilde{b}^2}, \tag{49}$$

where $\mathcal{R}_2 = 1 - \mathcal{R}_1$ from equation (36). For $a = 0$, the MN disc reduces to the Plummer (1911) sphere, and for $b = 0$ to the razor-thin Kuzmin (1956) disc; in the following, we indicate with $q_2 = a/b$ the disc flattening parameter. As in JJE models, we add the spherical NFW halo in equation (47), and a central BH, so that the resulting multicomponent models are completely determined once the values of ξ_1, q_1, $\mathcal{R}_1$, Υ_{*1}, k_1 for ρ_{*1}, $\tilde{b}$, q_2, Υ_{*2}, k_2 for ρ_{*2}, ξ_h, c, $\mathcal{R}_h$ for ρ_h, and $\mathcal{R}_{BH}$ for the BH, are assigned, in addition to the total stellar mass M_* and the scale length r_* (see Table 2). In Section 4.2.1, we consider the case of a dominant MN disc, when the ellipsoidal Jaffe component can be interpreted as the stellar halo of a disc galaxy, and in Section 4.2.2 the case of a small and counter-rotating stellar disc at the centre of a dominant stellar spheroid, as sometimes observed in real early-type galaxies (e.g. Morelli et al. 2004; Krajnović et al. 2015; Mitzkus, Cappellari & Walcher 2017; see also Cappellari 2016). The parameters of the DM halo and of the central BH are the same as in the JJE model.

4.2.1 *Results for the JHD model*

In the 'Jaffe–Heavy disc' JHD model (see Table 2), the ellipsoidal Jaffe stellar halo ρ_{*1} is characterized by a scale length $\xi_1 = 1$, a flattening $q_1 = 0.8$, a stellar mass fraction of 30 per cent (i.e. $\mathcal{R}_1 = 0.3$), and a mass-to-light ratio $\Upsilon_{*1} = 6$. The dominant MN disc ρ_{*2} ($\mathcal{R}_2 = 0.7$) is quite flat ($q_2 = 10$), with $\tilde{b} = 0.1$, and a lower $\Upsilon_{*2} = 2$.

In the central row of Fig. 1, the scaled density distributions $\tilde{\rho}_{*1}$, $\tilde{\rho}_{*2}$, and $\tilde{\rho}_*$ are shown. The resulting isodensity contours of ρ_* would be classified as 'discy' near the equatorial plane, and as 'boxy' at large distance from the plane. The radial profiles of the density distributions (including the DM), in the equatorial plane, are shown

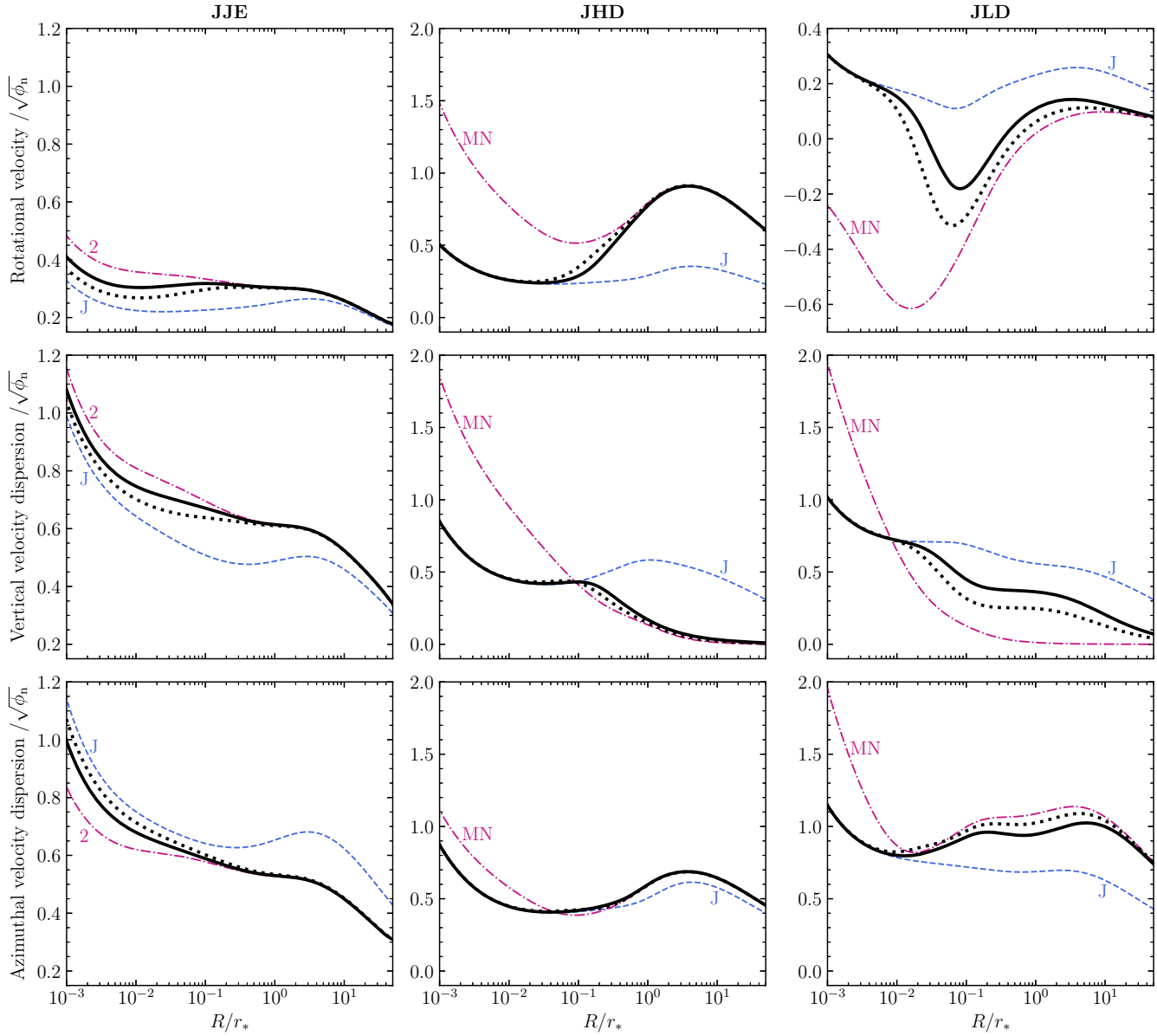

Figure 3. Radial profiles in the equatorial plane ($\tilde{z} = 0$) of the rotational velocities (top row), vertical velocity dispersions (middle row), and azimuthal velocity dispersions (bottom row), normalized to $\sqrt{\phi_n}$, for the three models of Table 2. Each panel shows the total mass-weighted (heavy solid) and luminosity-weighted (heavy dotted) fields, together with the corresponding fields of ρ_{*1} (dashed blue) and ρ_{*2} (dot–dashed magenta). Notice the different values on the vertical scales of the first column (JJE model) and of the top right panel showing the counter-rotation (JLD model).

in Fig. 2. It is apparent how, inside $\approx 0.1\, r_*$ the Jaffe halo dominates, around r_* the MN disc dominates, and ρ_h overcomes the total ρ_* outside $\approx 10\, r_*$. Note that, even if $\mathcal{R}_1 < \mathcal{R}_2$, ρ_{*1} dominates the total density in the central regions, due to the cuspy profile of the Jaffe density compared with the flat core of the MN density. The density decomposition reflects on the circular velocity profiles in the bottom panel of the same figure: the total υ_c at small radii is totally dominated by the BH, and at large radii by the DM halo; while the 'bump' around $3\, r_*$ is due to the MN and the DM potentials.

The radial profiles in the equatorial plane of the velocity fields, obtained from the Jeans equations, are shown in the middle column of Fig. 3, where from top to bottom the total mass- and luminosity-weighted rotational velocity, vertical velocity dispersion, and azimuthal velocity dispersion are plotted together with the corresponding quantities for each stellar component separately. For the adopted values of the parameters in Table 2, Δ_1 turns out to be negative in a quite central region, while $\Delta_1 + \sigma_1^2$ is everywhere positive; we decided to apply the generalized k-decomposition in equation (18) to both stellar components, with $k_1 = 0.5$ and $k_2 = 0.8$. The total velocity profiles, in the central regions, are completely determined by the Jaffe profile, because here $\rho_{*1} > \rho_{*2}$, compensating also for the higher Υ_{*1}; in the external regions, instead, the total profiles are dominated by the MN disc. Furthermore, υ_φ stays well below υ_c both in the inner and outer regions (see υ_c in Fig. 2), as a clear manifestation of *asymmetric drift* in the equatorial plane (e.g. BT08).

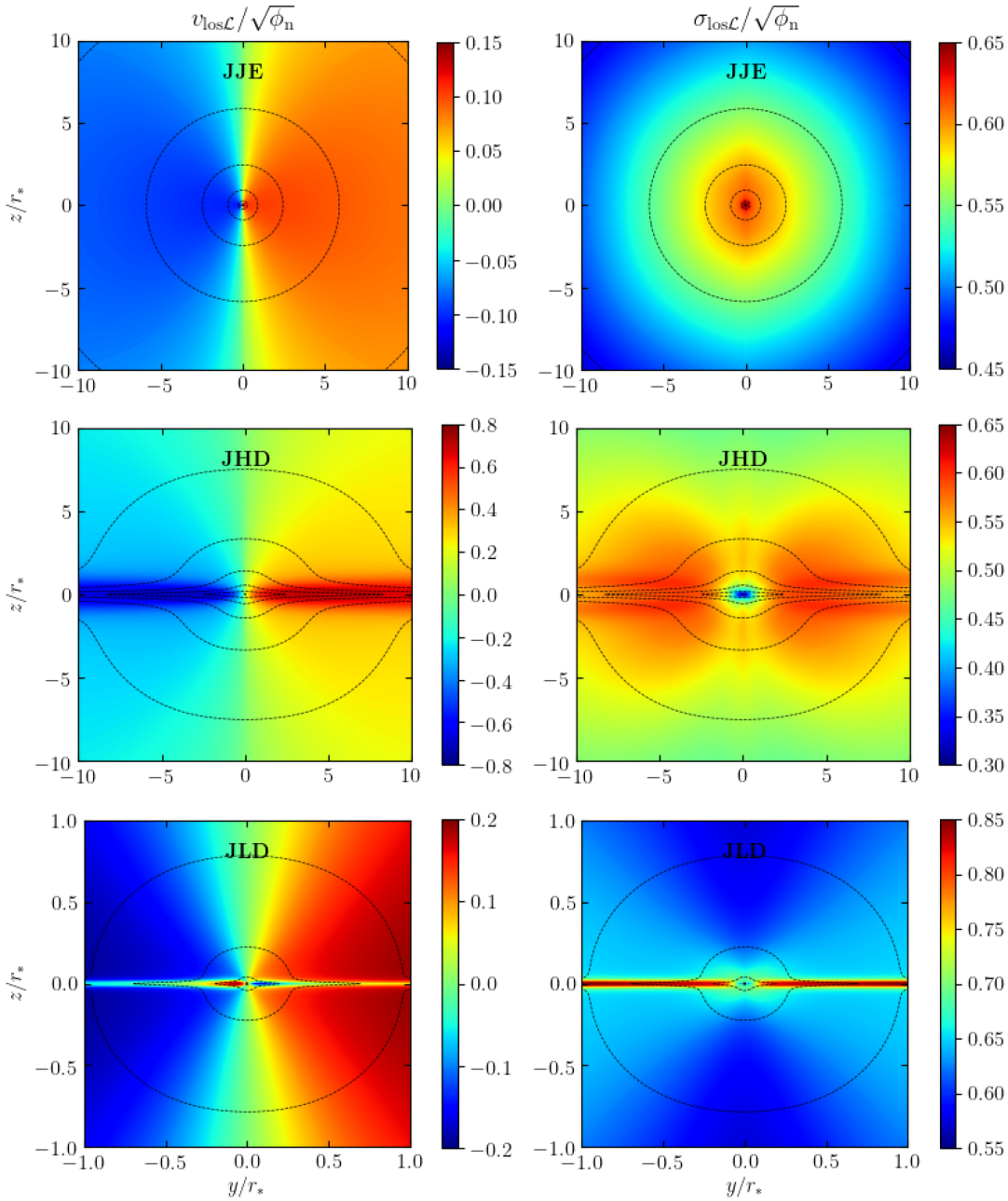

Figure 4. Edge-on projected luminosity-weighted rotational velocity $\upsilon_{\rm los\mathscr{L}}$ (left), and velocity dispersion $\sigma_{\rm los\mathscr{L}}$ (right), normalized to $\sqrt{\phi_{\rm n}}$, for the three models of Table 2. Notice the different ranges of values on the colourbars. For the JLD model, the region shown is limited to r_* to appreciate the central features, in particular the inner counter-rotating disc. The dotted contours show the galaxy isophotes with values spaced by 1 dex.

Note that σ_2, associated with a flat density profile at the centre, is much higher than σ_1, associated with $\rho_{*1} \sim R^{-2}$ in the inner regions, as can be expected from the integration of the vertical Jeans equation for a power law density distribution in the gravitational field of a point-mass (i.e. the BH). In addition, Δ_2 of the MN model with the central BH vanishes at the centre (see e.g. chapter 13 in Ciotti 2021), thus in the generalized k-decomposition, $\upsilon_{\varphi 2} \sim k_2\sigma_2$ (at variance with what would happen in the standard Satoh decomposition, i.e. $\upsilon_{\varphi 2} = k_2\sqrt{\Delta_2}$).

In the second row of Fig. 4, the luminosity-weighted projected fields $\upsilon_{\rm los\mathscr{L}}$ and $\sigma_{\rm los\mathscr{L}}$ are shown, and the high rotation of the disc is clearly visible. The drop of $\upsilon_{\rm los\mathscr{L}}$ inside r_* is due to a drop of the intrinsic rotational velocity (Fig. 3). Also $\sigma_{\rm los\mathscr{L}}$ shows the highest values near the equatorial plane, with a toroidal distribution around the centre, and a drop inside r_*.

4.2.2 *Results for the JLD model*

At variance with the JHD model, in the 'Jaffe-light disc' JLD model (see Table 2), the ellipsoidal Jaffe distribution ρ_{*1} accounts for almost the whole stellar mass of the galaxy ($\mathcal{R}_1 = 0.96$), while its scale length ($\xi_1 = 1$), flattening ($q_1 = 0.8$), and mass-to-light ratio ($\Upsilon_{*1} = 6$) are unchanged. The component ρ_{*2} is a small MN disc, with $\tilde{b} = 0.01$ and $\mathcal{R}_2 = 0.04$, while $q_2 = 10$ and $\Upsilon_{*2} = 2$ are the same of the JHD model.

Table 3. The parameters of the double-exponential disc and its 3MN fit from Smith et al. (2015). For the meaning of the parameters of the double-exponential disc, see Section 4.3.1 and Appendix B. For the 3MN model, we adopt the same notation of Section 4.2, with the same $\tilde{b}$ for all the three components, $q_i = \tilde{a}_i/\tilde{b}$, and $\mathcal{R}_i = M_{*i}/M_*$. The Jeans equations are solved in the isotropic case, with constant Satoh parameter $k = 1$.

Model	
Double-exponential disc	$\alpha = R_\mathrm{d}/r_* = 1$ $\beta = h/r_* = 0.1$ $\mathcal{R}_\mathrm{d} = 1$ $k = 1$
3MN fit (Smith et al. 2015)	$\tilde{b} = 0.12$ $q_1 = 4.64,\ q_2 = 21.42,\ q_3 = 18.67$ $\mathcal{R}_1 = 0.16,\ \mathcal{R}_2 = -5.77,\ \mathcal{R}_3 = 6.72$ $k = 1$

The scaled density distributions, and the resulting total stellar density, are shown in the three bottom panels of Fig. 1: $\tilde{\rho}_{*1}$ is (structurally) identical to that of the JHD model, while $\tilde{\rho}_{*2}$ is much more concentrated, so that the total stellar density is distributed in an extended halo with a very small disc. Indeed, the disc is almost invisible in the last panel, and it would be apparent only with a zoom in, as in Fig. 4. The last column of Fig. 2 shows the radial profiles in the equatorial plane of the density components, with their mass weights, and the resulting decomposition of the galaxy circular velocity profile. Notice that the central values of ρ_{*2} are higher than those in the JHD model, due to its smaller size, compensating for the reduced mass. In the circular velocity plot, this reflects into a larger contribution from the Jaffe component, and a smaller and inner 'bump' of the MN component. As a result, υ_c is almost flat between $10^{-2}\,r_*$ and $10\,r_*$.

In the last column of Fig. 3, the radial profiles of the velocity fields in the equatorial plane are shown. As in the previous models, of course, the total luminosity-weighted profiles, when distinguishable from the mass-weighted ones, are always closer to the profiles of the component with the smaller mass-to-light ratio. For the JLD model, both Δ_1 and Δ_2 are everywhere positive, so we apply the standard Satoh decomposition. The stellar halo is modelled as a slow rotator with $k_1 = 0.5$, while the circumnuclear stellar disc as a faster and counter-rotating light disc. In order to have counter-rotation limited to a central region, we adopt a position-dependent Satoh parameter, defined as follows:

$$k_2(R, z) = k_0 + (k_\infty - k_0)\frac{r}{r + 0.1 r_*}, \quad r = \sqrt{R^2 + z^2} \tag{50}$$

(e.g. Ciotti et al. in preparation; see also Negri et al. 2014a for an alternative parametrization), with $k_0 = -0.8$, $k_\infty = 0.1$, where the negative sign of k_0 assures the counter-rotation of the disc, as can be seen in the top right panel of Fig. 3. At very small radii (inside $10^{-2}\,r_*$), the total rotational velocity is positive because the density is dominated by the Jaffe component. We stress that the module of $\upsilon_{\varphi 2}$ decreases towards the centre, at variance with the JHD model, because now $\upsilon_{\varphi 2} = k_2\Delta_2$, and $\Delta_2 \to 0$, as explained in the previous Section. The central total vertical velocity dispersion is higher than that of the JHD model, even if the Jaffe component is structurally identical, because of the higher $\mathcal{R}_1$ and of the more concentrated MN disc.

In the last row of Fig. 4, the los luminosity-weighted velocities show clearly the effect of the inner thin disc; the region shown is limited to r_* to appreciate the central features. In particular, in the $\upsilon_{\mathrm{los}\mathscr{L}}$ distribution we have counter-rotation at small radii (but not in the very centre). The disc is also responsible for the highest values of the $\sigma_{\mathrm{los}\mathscr{L}}$ in the equatorial plane, and the extended surrounding toroidal distribution is also present, in analogy with the JHD model.

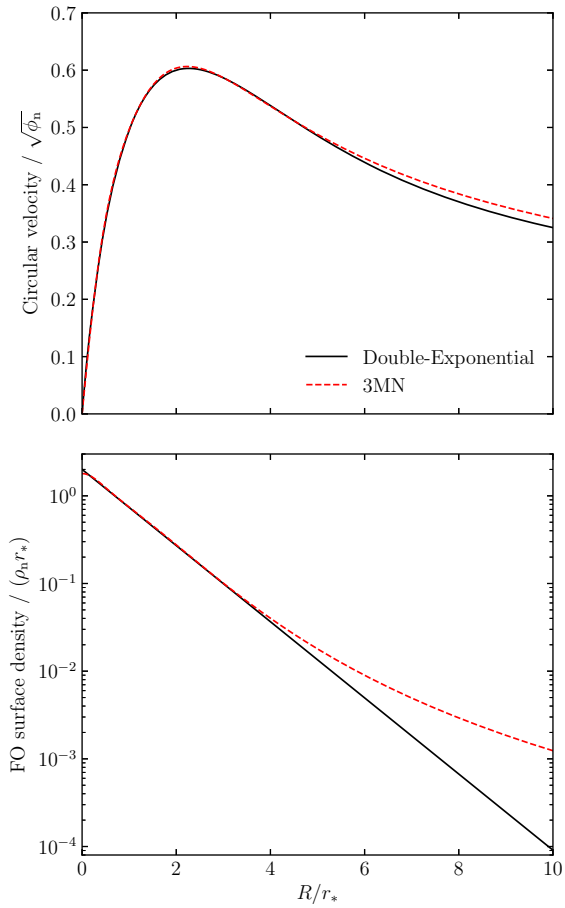

Figure 5. Circular velocity (top) and face-on surface density (bottom) profiles of the two models of Table 3; these plots can be compared with figs 3 and 7 in Smith et al. (2015).

4.3 Exponential discs and multi-MN decompositions

Exponential discs are the common choice for modelling disc galaxies. Their gravitational potential can be constructed numerically by using the general formula based on complete elliptic integrals, or by using Bessel functions. The latter approach is particularly useful in case of factorized densities, such as

$$\rho_*(R, z) = \rho_0 \mathrm{e}^{-R/R_\mathrm{d}} V(|z|/h), \tag{51}$$

where the function V describes the vertical structure of the disc, and R_d and h are respectively its scale length and scale height; the razor-thin exponential disc of central surface density Σ_0 is obtained for $V = \delta(z/h)$ and $\rho_0 = \Sigma_0/h$. Two natural generalizations of the infinitely thin exponential disc are obtained when V is also an exponential function (double-exponential disc) or some negative power of the cosh function ('pseudo-isothermal' exponential disc).

Unfortunately, the gravitational potential of these discs cannot be obtained analytically; however, due to their relevance in the construction of galaxy models, alternative models with analytical

potential have been proposed. In particular, the possibility to use multicomponent MN models to reproduce exponential discs, over some finite radial range, has been explored for example by Smith et al. (2015) and Rojas-Niño et al. (2016) (see also Ciotti & Pellegrini 1996; Flynn, Sommer-Larsen & Christensen 1996). Such alternatives optimize the fit of the density profile, and produce a good agreement with the circular velocity profile of the exponential disc. Obviously, the superposition of MN discs with their power-law radial decay at large radii (equation 48) cannot reproduce the exponential decay of equation (51). This forces to include at least one MN density component with negative mass (or negative scale length), that can lead to a disc density distribution somewhere negative. The use of a multicomponent MN representation of an exponential disc is motivated by the advantage of avoiding a time-consuming numerical computation of its gravitational potential. However, as we show in Appendix B, it is possible to obtain the potential of factorized exponential discs in equation (51) also with a very fast one-dimensional integration in terms of Bessel functions (a method we implemented in JASMINE2).

As a last and natural application of our procedure, we extend the work carried out by Smith et al. (2015) by constructing the solutions of the Jeans equations for the double-exponential disc and for its everywhere positive density representation in terms of three MN discs (hereafter 3MN). This 3MN decomposition is an ideal application of our modelling procedure, in particular because one MN component has negative mass, which gives the opportunity to illustrate how the scaling scheme in Section 3 works also with negative values of the mass ratios $\mathcal{R}_i$.

4.3.1 Results for a double-exponential disc and its 3MN fit

We consider the single-component double-exponential model in equation (B3), with mass $\mathcal{R}_\mathrm{d} = M_\mathrm{d}/M_* = 1$, scale length $\alpha = R_\mathrm{d}/r_* = 1$, and scale height $\beta = h/r_* = 0.1$. For this density, we build the everywhere positive 3MN fit, following section 2.2 in Smith et al. (2015). Accordingly, the three MN components (in our notation of equation 48) have the same scale height $\tilde{b}$, but different $\mathcal{R}_i$ and scale length $\tilde{a}_i$ ($i = 1, 2, 3$); in particular, from their fig. 5, we obtain $\tilde{b} = 0.12$, and from their equation (7) the values of $\mathcal{R}_i$ and $\tilde{a}_i$. The parameters for the double-exponential disc and for its 3MN fit are summarized in Table 3.

We compute the potential for the double-exponential disc both with the standard method in equation (42) and with the much faster integration of equation (B1), finding perfect agreement. As a safety check of the reconstructed 3MN model, we compare the circular velocity in the equatorial plane of the double-exponential disc and of its 3MN fit (Fig. 5, top panel), that can be compared with fig. 3 of Smith et al. (2015), and the FO surface density profiles of the two models (Fig. 5, bottom panel) that in turn can be compared with their fig. 7. The circular velocity of the exponential disc is almost perfectly reproduced over the explored radial range, while the reproduction of the FO surface density is less satisfactory, an unavoidable consequence of the everywhere positive decomposition adopted. For completeness, in Fig. 6, we present the EO surface density distributions of the two models. As expected, the two distributions are quite different in the outer regions, especially for increasing distance from the equatorial plane, where the 3MN model produces higher surface density values. Consequently, also the kinematical fields obtained from the solution of the Jeans equations are expected to show significant differences, especially at high $|z|$.

We use our procedure in JASMINE2 to evaluate these differences, a problem left open by the studies of Smith et al. (2015) and Rojas-Niño et al. (2016); we adopt for simplicity the case of the isotropic rotator, without a DM halo and a central BH. In Fig. 7, the EO projected rotational velocity and velocity dispersion are shown. The fields υ_los of the two models look remarkably similar, also outside the equatorial plane. In particular, the per cent error of the 3MN model with respect to the double-exponential model, in the equatorial plane, is < 9 per cent out to $4\,R_\mathrm{d}$, and < 14 per cent out to $10\,R_\mathrm{d}$. This quite satisfactory result is not obvious a priori, since υ_φ, at variance with υ_c, is not a function of the potential only, but it also depends on the velocity dispersion via the asymmetric drift. Therefore, the excellent agreement of υ_c in Fig. 5 is not a guarantee that also υ_φ, and its projection υ_los, are well reproduced by the 3MN density fit. The reproduction of υ_los outside the equatorial plane is still quite good, with a slightly higher discrepancy at increasing $|z|$, as expected, but improving for larger galactocentric distances; for example, at $z = R_\mathrm{d}$, the per cent error is < 23 per cent out to $4\,R_\mathrm{d}$, reducing to < 18 per cent out to $10\,R_\mathrm{d}$. The situation is different for σ_los: the two fields are significantly different, even in the equatorial plane, with the 3MN model showing values up to a factor of 2 larger than those of the double-exponential model. Moreover, the velocity dispersion of the 3MN model near the rotation axis presents a characteristic hourglass-shaped distribution (see also Negri et al. 2014a), only barely detectable at the very centre for the double-exponential model. Notice that this feature is not observed in the maps of Fig. 4 for the JHD and JLD models, even if they also contain a MN component, due to the addition of a stellar halo and a DM halo, and to the different kinematical decompositions adopted (see also the discussion in Smet et al. 2015). These experiments suggest caution when adopting the 3MN representation to interpret the observed velocity dispersion of disc galaxies.

5 CONCLUSIONS

We presented the theoretical framework for an efficient Jeans modelling of multicomponent axisymmetric galaxies, and its numerical implementation in the code JASMINE2, significantly upgraded from its original version JASMINE (Posacki et al. 2013). In this framework, the models can include an arbitrary number of stellar components, with different structural, dynamical and stellar population properties, a DM halo, and a central BH. The structural and dynamical properties of each stellar component can be mass- or luminosity-weighted, and projected on the plane of the sky. The internal dynamics of each stellar component is implicitly described by a two-integral DF (in general different for each component), so that a phenomenological decomposition of the azimuthal velocity field must be chosen. For each component, we can adopt the Satoh (1980) k-decomposition, where $\upsilon_{\varphi i} = k_i\sqrt{\Delta_i}$, or a generalized k-decomposition, where $\upsilon_{\varphi i} = k_i\sqrt{\Delta_i + \sigma_i^2}$; furthermore, the parameter k_i can be constant or position dependent. The generalized decomposition allows for the modelling of systems with $\Delta_i < 0$ (as may happen for density distributions elongated along the symmetry axis). The presented scheme can be easily extended to more general velocity decompositions, such as that introduced by Cappellari (2008), where the underlying DF depends on three integrals of motion.

In the numerical implementation, the gravitational potential of the density components is computed by default in terms of complete elliptic integrals (equation 42), a very accurate but quite time-expensive approach, that can become impractical especially when

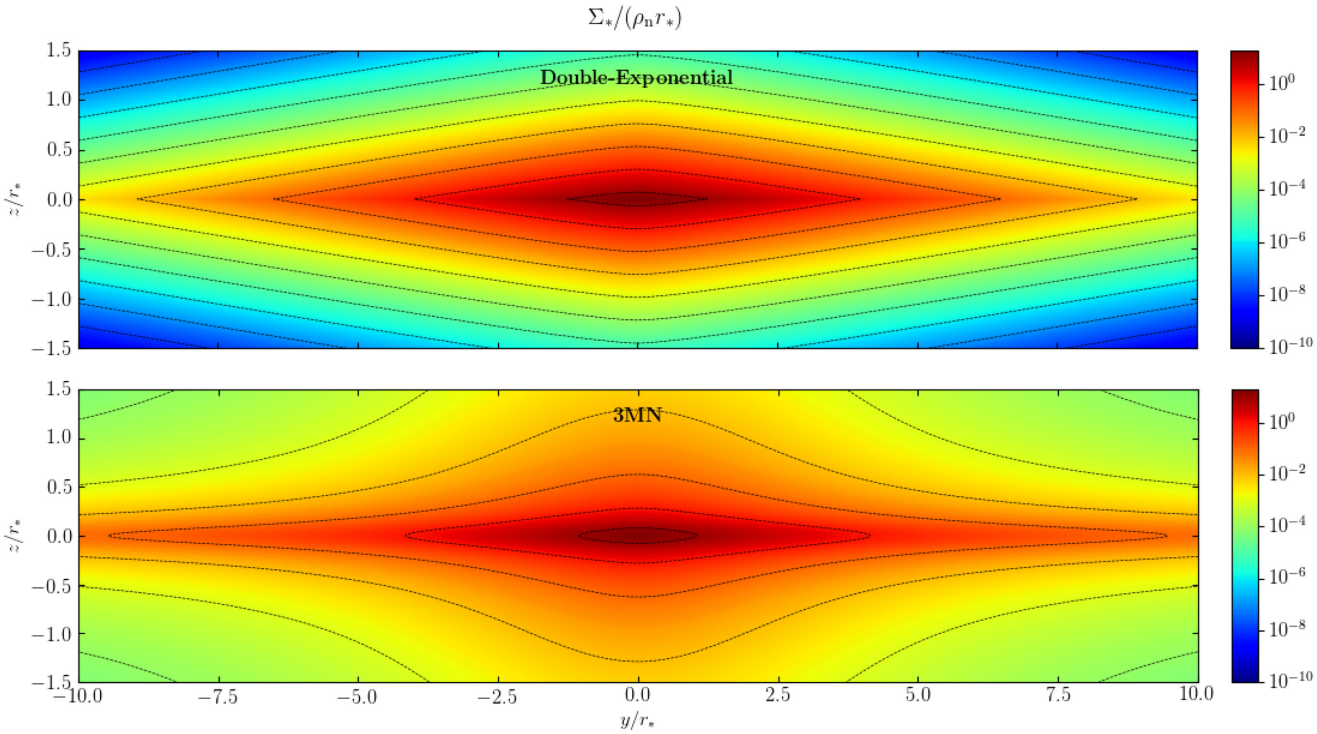

Figure 6. Edge-on surface density distributions Σ_* of the two models of Table 3. The dotted contours are spaced by 1 dex.

dealing with the exploration of the parameter space of multicomponent models. To reduce the computational time, we fully exploited the scalings allowed by the Poisson and the Jeans equations, and by the projection formulae. The resulting scheme led to an organization of JASMINE2 in two logically distinct parts: the Potential and Jeans Solver and the post-processing (PP). In practice, once the structural properties of the scaled stellar and DM distributions are assigned, the code computes, with a single run of the Potential and Jeans Solver, the scaled solutions of the Jeans equations, defining a *family* of models. The scaled Jeans solutions are then combined in PP, with the desired mass and luminosity weights, and the choice of appropriate kinematical decompositions, and then projected. The PP procedure can be performed several times, obtaining different specific models in the same family. Finally, for each model, the two physical scales M_* and r_* can be assigned. A further benefit of the presented approach is the possibility to gain a full understanding of the role of each density component in determining the resulting kinematical fields of the galaxy. For special density distributions, a further reduction of computational time is obtained by evaluating the potential with specific integral formulae, such as the Chandrasekhar formula for ellipsoidal distributions, and integrals involving Bessel functions for factorized disc distributions (see Appendix B).

In order to illustrate the features of our modelling procedure, we presented three galaxy models, composed of two stellar components, a spherical NFW DM halo and a central supermassive BH. In the JJE model, the total spherical stellar profile and one ellipsoidal stellar component, both Jaffe models, are assigned; the second stellar component is given by their difference. This model, when the DM halo is absent, has several properties available in analytical form (in particular in CMPZ21), and thus has been used to test the procedure and the code. The JHD model consists of a large and massive MN stellar disc, coupled with an ellipsoidal Jaffe stellar model, that can be seen as the stellar halo of a disc galaxy. In the JLD model, an ellipsoidal Jaffe component dominates in mass, and an MN stellar disc is small, inner and counter-rotating, as sometimes found in early-type galaxies.

As a fourth application, we explored the accuracy of one of the 3MN decompositions proposed by Smith et al. (2015) to reproduce the kinematical fields of double-exponential discs. We confirmed the excellent agreement of the rotation curves of the two models in the equatorial plane, at least out to $\sim 10R_d$. We also found that $\upsilon_{\rm los}$ tends to be larger for the double-exponential disc than for its 3MN representation, but overall the agreement is rather good, even outside the equatorial plane. A different situation is found for $\sigma_{\rm los}$: the values are significantly larger in the 3MN model, which also presents a characteristic hourglass-shaped vertical distribution. Some care is thus recommended when using a 3MN decomposition to infer the properties of observed disc galaxies.

Ongoing applications of the presented modelling procedure, and in particular of JASMINE2, include the building of multicomponent galaxy models for numerical simulations of gas flows in galaxies (e.g. Negri et al. 2014b; Gan et al. 2019a, b; Ciotti et al. in preparation); the study of circumnuclear stellar discs (also with counter-rotation, see e.g. Morelli et al. 2004; Krajnović et al. 2015; Mitzkus et al. 2017; Sormani et al. 2020; see also Cappellari 2016); a systematic exploration of galaxy models constrained to lie on the major observed Scaling Laws, extending the statistical approach pioneered in Bertin, Ciotti & Del Principe (2002) and Lanzoni & Ciotti (2003).

ACKNOWLEDGEMENTS

We are grateful to Antonio Mancino for independent checks of the results of JJE models. We thank the anonymous referee for useful comments that improved the paper.

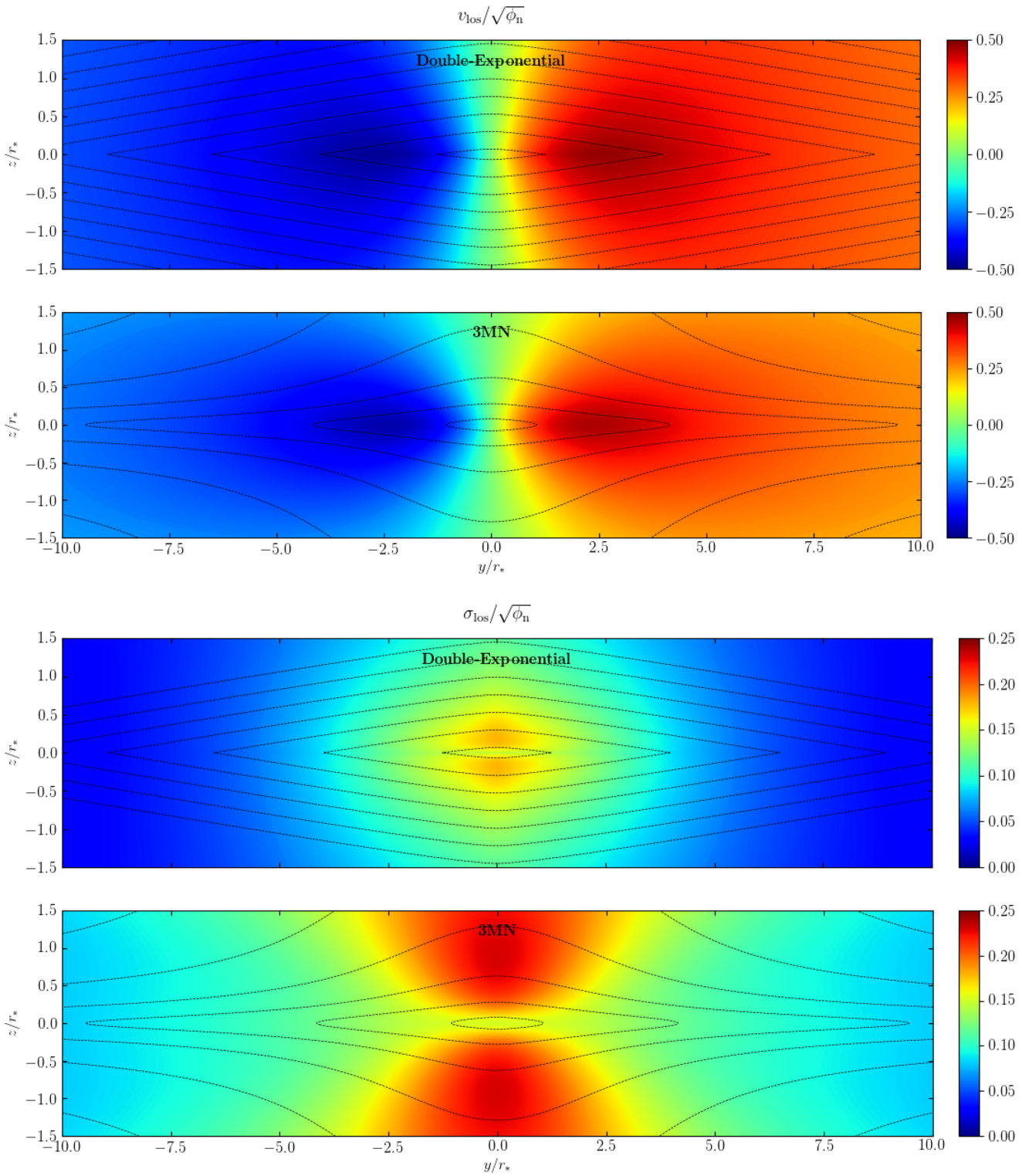

Figure 7. Edge-on projected rotational velocity $v_{\rm los}$, and velocity dispersion $\sigma_{\rm los}$, normalized to $\sqrt{\phi_{\rm n}}$, for the two models of Table 3. The dotted contours are the same as in Fig. 6.

DATA AVAILABILITY

The data underlying this article were produced by the authors. They will be shared under reasonable request to the corresponding author.

REFERENCES

Bertin G., 2014, Dynamics of Galaxies. Cambridge Univ. Press, Cambridge
Bertin G., Ciotti L., Del Principe M., 2002, A&A, 386, 149
Binney J., Tremaine S., 2008, Galactic Dynamics, 2nd edn. Princeton Univ. Press, Princeton (BT08)

Cappellari M., 2008, MNRAS, 390, 71
Cappellari M., 2016, ARAA, 54, 597
Caravita C., 2022, PhD thesis, Bologna University
Ciotti L., 2021, Introduction to Stellar Dynamics. Cambridge Univ. Press, Cambridge
Ciotti L., Bertin G., 2005, A&A, 437, 419
Ciotti L., Pellegrini S., 1996, MNRAS, 279, 240
Ciotti L., Mancino A., Pellegrini S., Ziaee Lorzad A., 2021, MNRAS, 500, 1054 (CMPZ21)
Flynn C., Sommer-Larsen J., Christensen P. R., 1996, MNRAS, 281, 1027
Gan Z., Ciotti L., Ostriker J. P., Yuan F., 2019a, ApJ, 872, 167
Gan Z., Choi E., Ostriker J. P., Ciotti L., Pellegrini S., 2019b, ApJ, 875, 109
Jaffe W., 1983, MNRAS, 202, 995
Kormendy J., Ho L. C., 2013, ARA&A, 51, 511
Krajnović D. et al., 2015, MNRAS, 452, 2
Kuzmin G. G., 1956, AZh, 33, 27
Lanzoni B., Ciotti L., 2003, A&A, 404, 819
Maraston C., 2005, MNRAS, 362, 799
Mitzkus M., Cappellari M., Walcher C. J., 2017, MNRAS, 464, 4789
Miyamoto M., Nagai R., 1975, PASJ, 27, 533
Morelli L. et al., 2004, MNRAS, 354, 753
Navarro J. F., Frenk C. S., White S. D. M., 1996, ApJ, 462, 563
Negri A., Ciotti L., Pellegrini S., 2014a, MNRAS, 439, 823
Negri A., Posacki S., Pellegrini S., Ciotti L., 2014b, MNRAS, 445, 1351
Plummer H. C., 1911, MNRAS, 71, 460
Posacki S., Pellegrini S., Ciotti L., 2013, MNRAS, 433, 2259
Renzini A., Buzzoni A., 1986, Global Properties of Stellar Populations and the Spectral Evolution of Galaxies. In Chiosi C., Renzini A., pp 195 – - 235, Spectral Evolution of Galaxies. Astrophysics and Space Science Library, vol 122, Springer Netherlands, Dordrecht
Rojas-Niño A., Read J. I., Aguilar L., Delorme M., 2016, MNRAS, 459, 3349
Satoh C., 1980, PASJ, 32, 41
Smet C. O., Posacki S., Ciotti L., 2015, MNRAS, 448, 2921
Smith R., Flynn C., Candlish G. N., Fellhauer M., Gibson B. K., 2015, MNRAS, 448, 2934
Sormani M. C., Magorrian J., Nogueras-Lara F., Neumayer N., Schönrich R., Klessen R. S., Mastrobuono-Battisti A., 2020, MNRAS, 499, 7
Yoon D., Yuan F., Ostriker J. P., Ciotti L., Zhu B., 2019, ApJ, 885, 16

APPENDIX A: POSITIVITY CONDITION FOR JJE MODELS

The stellar component ρ_{*2}, for the two-component ellipsoidal models described in Section 4.1, is given by the difference of an assigned total ρ_* and an assigned ρ_{*1}. This approach naturally leads to discuss the positivity of ρ_{*2}, with a treatment similar to that followed in the appendix of CMPZ21, and references therein. We generalize equation (46) as

$$\frac{\rho_{*2}(R,z)}{(3-\gamma)\rho_{\rm n}} = \frac{\xi}{qm^{\gamma}(\xi+m)^{4-\gamma}} - \frac{\mathcal{R}_1\xi_1}{q_1 m_1^{\gamma}(\xi_1+m_1)^{4-\gamma}}, \tag{A1}$$

recovering the case of JJE models for $\gamma = 2$. In order to discuss the positivity condition for ρ_{*2}, we use spherical coordinates, so that $(R, z) = r(\sin\theta, \cos\theta)$ and

$$m = s\Omega, \quad m_1 = s\Omega_1, \quad s \equiv \frac{r}{r_*}, \tag{A2}$$

where

$$\Omega^2 \equiv \sin^2\theta + \frac{\cos^2\theta}{q^2}, \quad \Omega_1^2 \equiv \sin^2\theta + \frac{\cos^2\theta}{q_1^2}. \tag{A3}$$

The positivity of ρ_{*2} reduces to a condition on $\mathcal{R}_1$, given by

$$\mathcal{R}_1 \le \mathcal{R}_{\rm M} \equiv \inf_{\mathcal{I}} \left[\frac{\xi q_1}{\xi_1 q}\left(\frac{\Omega_1}{\Omega}\right)^{\gamma}\left(\frac{\xi_1+s\Omega_1}{\xi+s\Omega}\right)^{4-\gamma}\right], \tag{A4}$$

over the rectangular region $\mathcal{I} \equiv \{s \ge 0, 0 \le \theta \le \pi/2\}$ in the (s, θ) plane. Following the discussion in CMPZ21, we determine

$$\mathcal{R}_{\rm M} = \min\left(\mathcal{R}_{\rm c}, \mathcal{R}_{\infty}, \mathcal{R}_0, \mathcal{R}_{\pi/2}, \mathcal{R}_{\rm int}\right), \tag{A5}$$

where the first four quantities refer to the minimum value of the r.h.s. of equation (A4) over the boundaries of $\mathcal{I}$, and $\mathcal{R}_{\rm int}$ is the value of a minimum (if it exists) in the interior of $\mathcal{I}$. When $q_1 \ne q$, it is simple to show that no critical points can exist in the interior of $\mathcal{I}$, and so the discussion reduces to the boundaries of $\mathcal{I}$: geometrically, $\mathcal{R}_{\rm M}$ can be reached only at the centre ($s = 0$, $\mathcal{R}_{\rm c}$), at infinity ($s \to \infty$, $\mathcal{R}_{\infty}$), along the symmetry axis ($\theta = 0$, $\mathcal{R}_0$), or on the equatorial plane ($\theta = \pi/2$, $\mathcal{R}_{\pi/2}$).

We begin with $\mathcal{R}_{\rm c}$ and $\mathcal{R}_{\infty}$, obtaining

$$\mathcal{R}_{\rm c} = \frac{\xi_1^{3-\gamma} q_1}{\xi^{3-\gamma} q} \min_{0\le\theta\le\pi/2}\left(\frac{\Omega_1}{\Omega}\right)^{\gamma}, \tag{A6}$$

$$\mathcal{R}_{\infty} = \frac{\xi q_1}{\xi_1 q} \min_{0\le\theta\le\pi/2}\left(\frac{\Omega_1}{\Omega}\right)^{4}. \tag{A7}$$

Now, from equation (A3), it is easy to show that for a generic $\alpha \ge 0$, the function $(\Omega_1/\Omega)^{\alpha}$ reaches its minimum at $\theta = \pi/2$ if $q_1 \le q$, and at $\theta = 0$ if $q \le q_1$, so that

$$\min_{0\le\theta\le\pi/2}\left(\frac{\Omega_1}{\Omega}\right)^{\alpha} = \begin{cases} 1, & q_1 \le q, \\ \left(\dfrac{q}{q_1}\right)^{\alpha}, & q \le q_1, \end{cases} \tag{A8}$$

and the conditions in equations (A6) and (A7) can be finally summarized as

$$\mathcal{R}_{\rm c} = \frac{\xi_1^{3-\gamma} q_1}{\xi^{3-\gamma} q} \min\left(1, \frac{q^{\gamma}}{q_1^{\gamma}}\right), \tag{A9}$$

$$\mathcal{R}_{\infty} = \frac{\xi q_1}{\xi_1 q} \min\left(1, \frac{q^{4}}{q_1^{4}}\right). \tag{A10}$$

Along the symmetry axis, and in the equatorial plane, condition (A4) becomes

$$\mathcal{R}_0 = \frac{\xi q^3}{\xi_1 q_1^3} \inf_{0\le s<\infty}\left(\frac{\xi_1 q_1 + s}{\xi q + s}\right)^{4-\gamma}, \tag{A11}$$

$$\mathcal{R}_{\pi/2} = \frac{\xi q_1}{\xi_1 q} \inf_{0\le s<\infty}\left(\frac{\xi_1 + s}{\xi + s}\right)^{4-\gamma}, \tag{A12}$$

and simple algebra finally shows that the results can be summarized as

$$\mathcal{R}_0 = \frac{\xi q^3}{\xi_1 q_1^3} \min\left[1, \left(\frac{\xi_1 q_1}{\xi q}\right)^{4-\gamma}\right], \tag{A13}$$

$$\mathcal{R}_{\pi/2} = \frac{\xi q_1}{\xi_1 q} \min\left(1, \frac{\xi_1^{4-\gamma}}{\xi^{4-\gamma}}\right). \tag{A14}$$

For the JJE models in Section 4.1, with $\xi_1 < \xi$, $q_1 < q$, and $\gamma = 2$, the positivity condition (A5) becomes

$$\mathcal{R}_1 \le \mathcal{R}_{\rm M} = \frac{\xi_1 q_1}{\xi q}. \tag{A15}$$

APPENDIX B: POTENTIAL OF FACTORIZED EXPONENTIAL DISCS

Due to the importance in applications, here we summarize the main results about the numerical evaluation of the potential produced by factorized exponential discs as in equation (51), by using the technique of Bessel functions. From equations (2.103) and (2.114)

in Ciotti (2021), the potential can be easily written in full generality as

$$\phi(R,z) = -2\pi G\rho_0 r_*^2\alpha^2\beta\int_0^\infty \frac{\mathrm{J}_0(\lambda\tilde{R})\hat{V}(\lambda\beta,\tilde{z}/\beta)}{(1+\alpha^2\lambda^2)^{3/2}}\,\mathrm{d}\lambda, \tag{B1}$$

where J_0 is a Bessel function of the first kind, $\alpha = R_\mathrm{d}/r_*$, $\beta = h/r_*$, $\tilde{R} = R/r_*$, $\tilde{z} = z/r_*$, and finally

$$\hat{V}(\gamma,x) \equiv \int_{-\infty}^{\infty} \mathrm{e}^{-\gamma||x|-t|}V(|t|)\,\mathrm{d}t. \tag{B2}$$

Therefore, once the function $\hat{V}$ is known analytically, the integration for each grid point $(\tilde{R},\tilde{z})$ reduces to a fast one-dimensional integration, instead of the more time-consuming two-dimensional integration that would be required when using the standard formula based on complete elliptic integrals (equation 42), or the alternative equation based on modified Bessel functions (equation 2.170 in BT08; equation 4 in Smith et al. 2015).

For the three discs considered in Smith et al. (2015), we define $\mathcal{R}_\mathrm{d} = M_\mathrm{d}/M_*$, where M_d is the total mass of the disc, so that for the double-exponential disc considered in Section 4.3.1, we have

$$\rho_*(R,z) = \frac{\rho_\mathrm{n}\mathcal{R}_\mathrm{d}}{\alpha^2\beta}\mathrm{e}^{-\tilde{R}/\alpha-|\tilde{z}|/\beta},\quad \hat{V}(\gamma,x) = \frac{2(\gamma\mathrm{e}^{-|x|}-\mathrm{e}^{-\gamma|x|})}{\gamma^2-1}, \tag{B3}$$

for $\gamma \neq 1$, and $\hat{V}(1,x) = (1+|x|)\mathrm{e}^{-|x|}$. For completeness, we also report the formulae for the razor-thin exponential disc,

$$\rho_*(R,z) = \frac{2\rho_\mathrm{n}\mathcal{R}_\mathrm{d}}{\alpha^2\beta}\mathrm{e}^{-\tilde{R}/\alpha}\delta(\tilde{z}/\beta),\qquad \hat{V}(\gamma,x) = \mathrm{e}^{-\gamma|x|}, \tag{B4}$$

where δ is the Dirac-δ function, and for the 'pseudo-isothermal' exponential disc,

$$\rho_*(R,z) = \frac{2^{2-a}\rho_\mathrm{n}\mathcal{R}_\mathrm{d}}{\alpha^2\beta\,\mathrm{B}(a/2,a/2)}\frac{\mathrm{e}^{-\tilde{R}/\alpha}}{\cosh(\tilde{z}/\beta)^a},\quad a>0, \tag{B5}$$

where $B(x,y)$ is the Euler complete Beta function, and

$$\hat{V}(\gamma,x) = 2^{a-1}\mathrm{e}^{-\gamma|x|}B\left(\frac{a+\gamma}{2},\frac{a-\gamma}{2},\frac{\mathrm{e}^{2|x|}}{1+\mathrm{e}^{2|x|}}\right) + 2^{a-1}\mathrm{e}^{\gamma|x|}B\left(\frac{a+\gamma}{2},\frac{a-\gamma}{2},\frac{1}{1+\mathrm{e}^{2|x|}}\right). \tag{B6}$$

For computational reasons, it can be convenient to express the incomplete Beta functions above by using their hypergeometric expression

$$\mathrm{B}(a,b;z) = \frac{z^a}{a}\,{}_2F_1(a,1-b,1+a;z). \tag{B7}$$

We verified the numerical accuracy of the one-dimensional integration of equations (B1)–(B3) by comparison with the potential obtained from equation (42).

We conclude by noticing that equation (B1) can be immediately extended to other families of factorized thick discs, with a radial density factor allowing for an explicit Hankel transform. Examples of these thick discs (implemented in JASMINE2), are the Kuzmin disc, the truncated, untruncated and finite Mestel discs, the truncated constant density disc, and the Maclaurin disc (for the relative Hankel transform, see respectively equations 13.148, 2.119, 5.46, 5.55, 5.53, 5.54 in Ciotti 2021; see also Caravita 2022).

This paper has been typeset from a TEX/LATEX file prepared by the author.